



Assessing Tidal Hydrodynamics in a Tropical Seascape Using Structure-from-Motion Photogrammetry and 2D Flow Modelling

Cécile Vulliet^{1,2} · Jack Koci^{1,2} · Ben Jarihani³ · Marcus Sheaves^{1,2} · Nathan Waltham^{1,2}

Received: 12 April 2023 / Revised: 2 October 2023 / Accepted: 11 October 2023 / Published online: 29 October 2023
© The Author(s) 2023

Abstract

Tidal wetlands continue to be threatened by changes in seascape hydrological regime and connectivity resulting from human activities (e.g. urbanisation, engineered barriers) and climate change. Reliable and parsimonious models that can be used by managers and practitioners to simulate tidal wetland hydroperiod dynamics (duration, depth, and frequency of tidal inundation) at high-resolution are limited presumably because these ecosystems have very low elevation across their flooding plain. Here, we developed a two-dimensional hydrodynamic model parameterised using a high-resolution (3 cm) and accurate (8-cm RMSE elevation error) digital elevation model (DEM) and land cover map (2-cm resolution) derived from unoccupied aerial vehicles (UAVs) structure from motion photogrammetry (SfM) to assist in the understanding of tidal wetland hydroperiod and hydrological connectivity of an upper tidal Australian tropical seascape. Ground-based water level datasets were used to calibrate and validate the model with higher accuracy (RMSE = 7 cm between maximum observed and simulated depth). The high-resolution approach demonstrates how small changes in topography such as vehicle tracks can interfere with hydrological connectivity. Centimetre-changes in tidal height resulted in important variations (10 ha) in the total area of the wetland being inundated, suggesting that small anthropogenic modifications of tidal inputs (e.g. culverts and sea-level rise) might have important implications on tidal wetland inundation patterns. Despite challenges related to reconstructing topography in densely vegetated areas and obtaining bathymetric data, the method developed here represents an accurate and cost-effective approach to quantify tidal wetland hydroperiod. This approach assists in planning, defining, and implementing effective and measurable restoration and protection projects of tidal wetland ecosystems.

Keywords Tidal marshes · Hydroperiod · Unoccupied aerial vehicle (UAV) · Saltmarsh · Digital elevation models (DEMs) · Seascape connectivity

Introduction

Tidal wetlands (saltmarshes, mangroves, mudflats, and saltpans) are located at the land-sea boundary and hold significant ecological and economic value. For instance,

they provide critical resources to commercially targeted species (e.g. European seabass (*Dicentrarchus labrax*) and sea mullet (*Mugil cephalus*)) (Deegan et al. 2002; Raoult et al. 2018; McCormick et al. 2021), assist with nutrient processing (Rivera-Monroy et al. 2011), and are basal carbon sources supporting coastal food web production (Abrantes and Sheaves 2009; Connolly and Waltham 2015; Jinks et al. 2020). Tidal wetlands are also incredibly effective in absorbing greenhouse gas emissions (Wang et al. 2021a), thereby counteracting anthropogenic carbon emissions and mitigating climate change.

Despite recognition of their values, tidal wetlands continue to be jeopardised by direct ecosystem destruction and degradation (Murray et al. 2022) as a result of urbanisation and agriculture (Saintilan and Wilton 2001), including installation of engineered barriers (e.g. roads, culverts, and tidal gates) and coastal infrastructures (e.g. seawalls and dikes), which

Communicated by Dan Friess

✉ Cécile Vulliet
cecile.vulliet@my.jcu.edu.au

¹ TropWATER, Centre for Tropical Water and Aquatic Ecosystem Research, James Cook University, Bebegu Yumba, Townsville, QLD 4814, Australia

² College of Science and Engineering, James Cook University, Bebegu Yumba, Townsville, QLD 4814, Australia

³ University of the Sunshine Coast, School of Science Technology and Engineering, 90 Sippy Downs Drive, GoldCoast, QLD, Australia

alter inundation regimes, leading to modifications in seascape connectivity and configuration (e.g. vegetated patch distribution and structure) (Bishop et al. 2017; Rodríguez et al. 2017). Climate change (e.g. sea-level rise, changes in temperature and rainfall patterns, and extreme weather events) also modifies seascape connectivity patterns via changes in hydrological, morphological, and biological processes (Gilby et al. 2021; Colombano et al. 2021; Finotello et al. 2022), which can be exacerbated by human activities (Gedan et al. 2009). An example is the coastal squeeze effect where saltmarshes become reduced between urbanisation and mangroves migrating to higher elevations due to increases in mean sea level (Torio and Chmura 2013). Implementation of effective restoration projects and urban planning that minimise environmental loss is, therefore, urgently needed. However, this is constrained by a poor understanding of the location-specific tidal wetland hydroperiod nuances, which can be influenced by a combination of vegetation mosaic and impediment on ingress, inundation depth, and frequency of wetland inundation (Bradley et al. 2020; Karim et al. 2012; Ziegler et al. 2021; Waltham et al. 2021).

Tidal hydroperiod determines the depth, duration, and timing of flooding and, as a result, influences hydrological connectivity and, subsequently, many critical ecohydrological and morphodynamical processes such as the movement of biota throughout seascapes (Rozas 1995; Minello et al. 2003; Davis et al. 2014), soil-vegetation interactions (Liu et al. 2021), carbon sequestration (Wang et al. 2021b), and coastal erosion (Finotello et al. 2022). These processes ultimately contribute to coastal productivity and resilience (Olds et al. 2012); hence, tidal wetland restoration success can be closely linked with hydrological processes (Zhao et al. 2016). Tidal wetland hydroperiod is most strongly influenced by topography, but also by many hydrological, geomorphic, edaphic, biological, and climatic variables (Xin et al. 2022). Complex interactions among these factors mean, for managers, that hydroperiod is challenging to quantify accurately (Passeri et al. 2015).

Over the past decade, advancements have occurred in the development of techniques to examine hydroperiod and connectivity of these ecosystems within nearby estuaries and coasts. Direct measurement approaches have used water level loggers (or pressure loggers) deployed at single points in space (Peterson and Turner 1994; Davis et al. 2014) or along transects (Kumbier et al. 2021). For instance, Minello et al. (2012) used tidal gauge data, which was checked using point elevation measurements, to more accurately investigate spatial variability in saltmarsh hydroperiod. That study enabled comparisons of hydroperiod across multiple locations, but it still required manual water level measurements, which can be prone to measurement error.

There has been growing interest in using complex empirical and physical numerical models to understand tidal

wetland hydrodynamics, notably to recognise the relationships between hydrology, saltmarsh evolution, and morphology (Kirwan et al. 2010; Fagherazzi et al. 2013, 2020; Xin et al. 2013, 2022; Bouma et al. 2016). These models range from zero-dimensional (i.e. process at single points) (Allen 1995) to one-dimensional (e.g. channel transects) (D'Alpaos et al. 2007; Karim et al. 2014), two-dimensional (2D) (e.g. tidal wetland platform) (Temmerman et al. 2007; Alizad et al. 2016; Fleri et al. 2019; Finotello et al. 2022), and three-dimensional (3D) models that encompass multi-dimensional variability in hydrology and sediment transport (Kirwan and Murray 2007; Xin et al. 2022). There have also been attempts to combine these models (Moffett et al. 2012; Kumbier et al. 2022). For instance, Alizad et al. (2016) investigated saltmarsh response to sea-level rise by combining a 2D hydrodynamic model developed by Bacopoulos et al. (2012) that uses tides, wind, pressure, and bathymetric-topographic datasets to understand saltmarsh hydroperiod, with a zero-dimensional model of saltmarsh accretion and biomass productivity derived from Morris et al. (2002). While these models represent an important advancement in our ability to understand saltmarsh functioning, the complexity and high input data requirements may preclude their broader application by environmental scientists, ecologists, and practitioners, particularly in data-sparse situations.

Recent advances in remote sensing techniques, coupled with freely available modelling software with user-friendly graphical user interfaces (GUIs), are opening the door to readily applicable approaches to quantify tidal wetland hydroperiod dynamics and connectivity. These new approaches might be more easily communicated and integrated into tidal wetland studies (e.g. fish habitat uses) and restoration. For example, using 2D simulation software such as, but not limited to, MIKE 21 (Warren and Bach 1992), TELEMAC-2D (Morris et al. 2013), TUFLOW 2D (Syme 2001), Delft3D (Temmerman et al. 2005; Horstman et al. 2015), or HEC-RAS can offer a detailed spatial and quantitative understanding of tidal inundation with minimal data input (Symonds et al. 2016; Karim et al. 2021; Muñoz et al. 2021). The basic input for hydrodynamic models includes bathymetry or topographic datasets (digital elevation models (DEMs)), land cover to account for surface roughness, and water level or discharge time series. Nevertheless, the low-gradient and narrow-width (< 1 m) draining channels in coastal areas could be completely missed or mis-represented depending on DEM resolution and uncertainty level in data acquisition (Chassereau et al. 2011).

High- or very high-resolution DEMs (< 1 m) are traditionally developed using ground-based LASER scanners (Sampson et al. 2012) or LiDAR instruments (Goodwin and Mudd 2019) and recently, by using unoccupied aerial vehicle (UAV) technology (Shaad et al. 2016; Pinton et al. 2020; Zhu et al. 2019; Li et al. 2021; Annis et al. 2020). Structure-from-motion with multi-view stereophotogrammetry (SfM)

(e.g. Koci et al. 2020) has emerged as a low-cost alternative to UAV-LiDAR (0.6–40% of LiDAR cost (e.g. Hu et al. 2021)). UAV-SfM produces 3D point clouds and DEMs with comparable resolution and accuracy to that of LiDAR in most environments (Nouwakpo et al. 2016; Annis et al. 2020; McNicol et al. 2021). In addition to high-resolution topographic models, UAV-SfM generates high-resolution orthomosaic maps providing detailed information on surface features (e.g. vegetation, roads, and trails). UAV-SfM can thereby fulfil two essential data requirements for 2D hydrodynamic modelling (i.e. DEM and land cover) (Annis et al. 2020). This approach might be particularly useful in tidal wetlands characterised by low-relative gradient with yet complex topographies (e.g. tidal channels), where subtle variations in topography cannot be captured with coarse DEMs (Chassereau et al. 2011).

This study aimed to test the potential of a UAV-derived DEM with a 2D flow model to simulate inundation patterns in a tidal wetland. Specifically, the main purposes

of this study were (1) to attempt to parameterise a detailed hydrodynamic model of the upper region of an intertidal tropical seascape using a UAV-SfM-derived DEM, a UAV-SfM-derived land cover dataset, and tidal data; (2) to try to derive information on tidal wetland hydrological connectivity and quantify tidal wetland inundation extent, depth, and duration based on the hydrodynamic model outputs; (3) to investigate the importance of high-resolution DEMs in low relative relief; and (4) to assess the advantages and weaknesses of UAV-SfM to study tidal wetland hydroperiod.

Materials and Methods

Study Site

The study site is in the upper intertidal region of Blacksoil Creek in north Queensland, Australia (−19.297867, 147.021333), covering 82.54 ha (Fig. 1). The study site

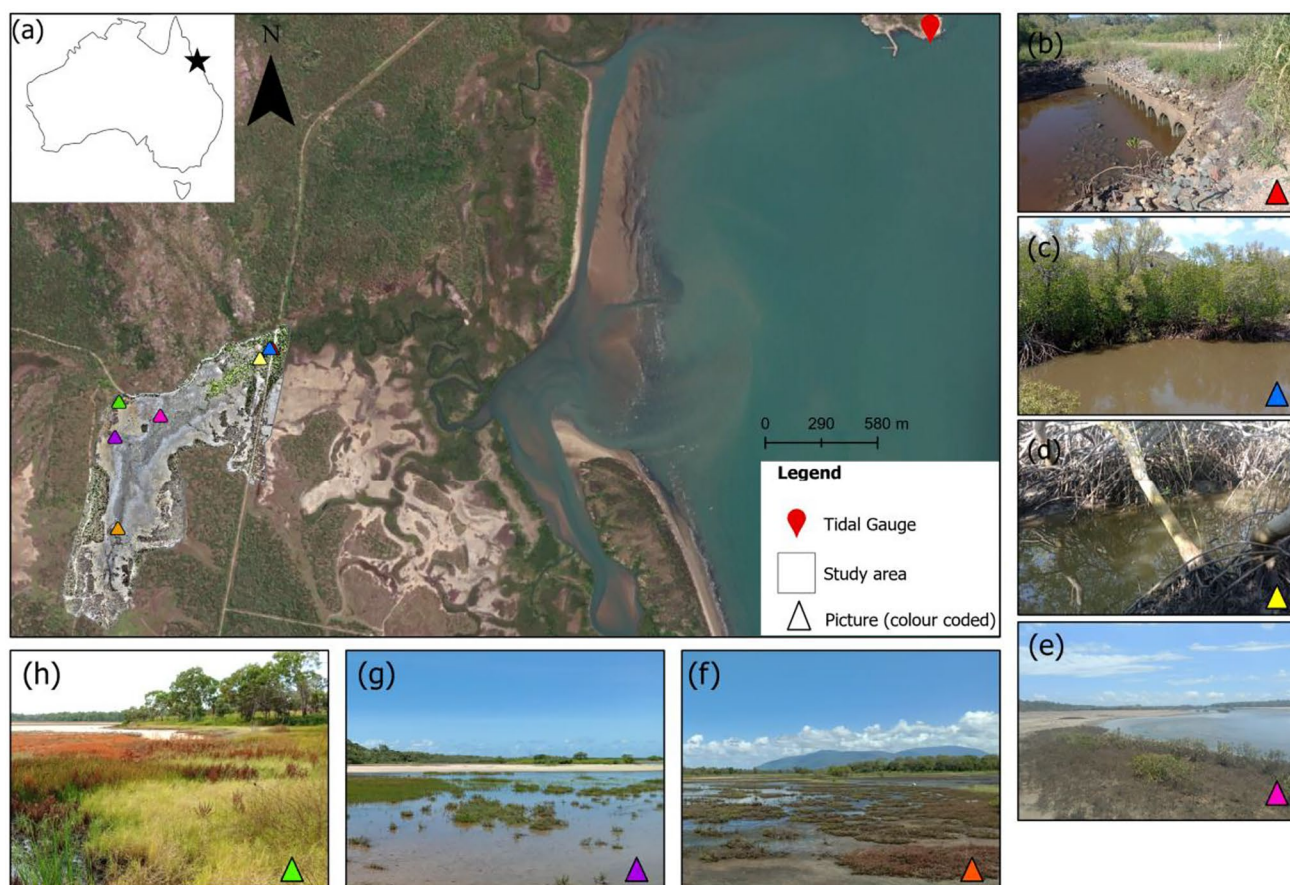


Fig. 1 **a** Study area map showing the location of the study site on the Australian East coast and location of tidal gauge; **b** photo of the culvert at the north-eastern boundary of the study site; **c** photo of the culvert (shown in **b**) during low tide bordered by *Rhizophora stylosa* and *Avicennia marina*; **d** tidal channel draining the upper portion of the site surrounded by *R. stylosa*; **e** succulent saltmarsh dominated

by *Sarcocornia quinqueflora* with encroaching *A. marina*; **f** succulent saltmarsh patches dominated by *S. quinqueflora*; **g** patches of herbaceous saltmarsh dominated by *Sporobolus virginicus*; and **h** herbaceous saltmarsh community at the transition between saltpan/saltmarsh and fully terrestrial vegetation (Software used: ArcGIS PRO)

represents a dry tropical estuarine complex consisting of mangrove forests dominated by the red mangrove (*Rhizophora stylosa*) at the seaward and channel edges transitioning to the grey mangrove (*Avicennia marina*) and the yellow mangrove (*Ceriops tagal*) in the upper intertidal area furthest from the open water channel. In the upper to supratidal zone, saltpans and saltmarshes dominate, including the bead weed (*Sarcocornia quinqueflora*) and the salt couch (*Sporobolus virginicus*).

There is no freshwater stream inflow; it only enters via groundwater and direct runoff during rain events. The estuary downstream of the study area is semi-diurnal mesotidal, with the highest tides occurring during the day in austral summer and night in austral winter. The Highest Astronomical Tide (HAT) is 3.84 m above the Lowest Astronomical Tide (LAT) datum (2.150 m above the Australian Height Datum (AHD)) (Queensland 2022). The 1991–2021 average tidal height is 1.72 m (Queensland 2022). The climate is dry-tropical, with most rainfall (900–1800 mm/annum) (Bruinsma 2001) occurring during the wet season (November–April). There is a road with a multi-pipe culvert (10 pipes of 1-m diameter) downstream of the study area on the main drainage creek (Fig. 1b). Four small (~40 cm of diameter) single-pipe culverts are found across the road, south of the main culvert.

Modelling Framework and Setup

The free software HEC-RAS 6.1 (Windows) was used to develop a 2D hydrodynamic model of the study site using the 2D unsteady diffusion-wave equations. HEC-RAS uses a high-resolution sub-grid system, allowing water movement in each cell to be strongly controlled by the terrain model (Shustikova et al. 2019). Although the diffusion wave equations are not recommended for tidally driven system and the shallow water equations should be used instead, the shallow water equations did not yield stable simulations. The data inputs were (1) UAV-derived DEM, (2) the land cover dataset with associated Manning's roughness coefficient values, and (3) tidal data corresponding to periods at which pressure loggers were deployed. The model was first built by manually delimiting the perimeters around the study site. The 2D flow areas were then generated using the "Computation Points with All Breaklines" tools with computation point spacing of 2 × 2 m, which generated an irregular mesh of 195,131 cells (mostly of 4 sides and up to 8 sides along mesh boundaries). The 3-cm resolution UAV-DEM (see below) was used to extract the sub-grid level information. To reduce computational time while keeping information on the high-resolution terrain, HEC-RAS uses a sub-grid bathymetry approach that enables the use of coarser grid size on finer terrain model (Brunner 2016; Shustikova et al.

2019). The approach consists of a pre-processing step that calculates hydraulic radius, volume, and cross-sectional area from the finer topographic data for each computational grid cells (Shustikova et al. 2019). This sub-grid bathymetry approach allows the information from the fine scale terrain model to be accounted for in the coarser grid through mass conservation (Casulli 2009; Brunner 2016). Hence, DEM resolution influences model accuracy (Yalcin 2018). For instance, Yalcin (2018) demonstrated that a decrease in the digital surface model (DSM) resolution (0.25–10 m/pixel) with the same grid size (2 m × 2 m) linearly increases depth and inundation area inaccuracies compared to the 2 m × 2 m grid size with a 0.0432-m DSM. By opposition, no notable differences in model accuracy were observed between simulations computed with the 0.0432-m DSM and grid sizes of 2 m × 2 m to 10 m × 10 m. An abrupt decrease in model performance was only observed with a grid size equal to or greater than 15 m × 15 m. Numerical details on the sub-grid bathymetry approach used by HEC-RAS can be found in Brunner (2016).

The boundary condition (tidal flow data) was implemented using the stage hydrograph with the initial stage used. The initial conditions were left blank. Only one boundary condition was used, which was placed manually downstream of the culvert in the main channel, outside of the 2D flow area, which is presented in the supplementary materials (Fig. S2). Note that tides only enter to the study site via the culverts found across the road at the eastern boundary of the study site (Fig. 1).

Input Data

UAV-Derived DEM

UAV surveys were conducted over 2 days in September 2021. A DJI Phantom 4 RTK (Real-Time Kinematic) (SZ DJI Technology Co., Ltd.) connected to a DJI RTK Base Station set over a known benchmark was flown at 60-m altitude (62-m ground sample distance) on a one-grid mission planned to use the DJI RTK App (SZ DJI Technology Co., Ltd.). The camera model was FC6310R with maximum image size of 5472 × 3648, focal length of 8.8 mm, and pixel size of 2.41 × 2.41 μm. Full specifications of the Phantom 4 RTK can be assessed on the official DJI website (<https://ag.dji.com/fr/phantom-4-rtk/specs>). Images were collected at nadir with 85% side and forward image overlap. The UAV was flown each day between 9:30 and 15:00, with short interruptions to change the battery (i.e. each flight was approximately 20–25 min) totalling to 6488 images. RTK-GPS measurements recorded by the UAV ended up not being used for data processing due to the difficulties and time limitations in finding a workflow leading to high accuracies.

Thirty-three ground control points (GCPs) were evenly distributed in the corner, along the boundary, and across the study site to maximise DEM accuracy (Sanz-Ablanedo et al. 2018). The GCPs consisted of rectangular black and white checkerboards of 60 cm × 60 cm. To georeference the model with centimetre-level accuracy (Koci et al. 2017; Taddia et al. 2021), the centre of the GCPs were surveyed with Real-Time Kinematic-Global Positioning System (RTK-GPS) (CHC i80) (Shanghai HuaCe Navigation Technology Ltd.) (taking the average of 10 readings) (Fig. 2a). The accuracy of the RTK-GPS was calculated using the GCPs (33) and validation points (562, see details below), resulting in an RTK-GPS mean horizontal error of 0.015 ± 0.000 m (standard error (SE)) (standard deviation (SD) of 0.005 m) and mean vertical error of 0.027 ± 0.000 m (SD of 0.009 m). The coordinates were recorded in the GDA2020 MGA zone 55 reference system and orthometric elevation in the Australian Height Datum (AHD). Agisoft Metashape (Agisoft LLC) was used to create dense point clouds and orthomosaics from UAV-SfM. The DEM was generated following dense point cloud classification of ground points. Point cloud density (calculated as the total of points divided by the total area surveyed) was 4.81 points per m². Detailed processing steps and parameters are provided in Table 1.

The DEM was exported towards ArcGIS Pro 2.8.6 (Esri) for further cleaning of above-ground control points and reconstruction of the main channel. Dense vegetation cover precluded accurate reconstruction of the channel bathymetry using aerial imagery in those areas where mangrove forest did not allow the survey of ground points. In addition, the RTK-GPS received no to very low signal in the mangrove forest. Hence, in these areas, on-ground GPS points (Garmin hand-held GPS) were taken along the channel banks, in addition to five cross-sectional profiles of the channel surveyed with RTK-GPS. The low RTK signal in the mangrove forest prevented additional cross-sectional profiles. It is noted that GPS accuracy is low compared to RTK-GPS (5–15 m horizontal error), which added to uncertainties in channel delimitation and reconstruction (see Discussion). Channel bathymetry was reconstructed using Natural Neighbor (or Sibson) interpolation (the “Interpolate from the Edge” tool in ArcGIS Pro). This interpolation technique creates a smooth surface using a local and spatially adaptive method that retains the original values at the reference points (Etherington 2020). This tool was also used to remove mangrove trees. A conservative terrain filter tool (available in the Pixel Editor tools) that detects and removes above ground points while conserving natural slopes was used to remove remaining vegetation from the DEM surface. The DEM was hydrologically corrected (Jarihani et al. 2015) using the “Fill” tool. Elevation accuracy was assessed by comparing extracted values from the elevation raster to the elevation of 562 RTK-GPS random validation points (the number was

not initially set but the aim was to collect the maximum number of RTK-GPS validation points across the study site during the allocated time). DEM error is expressed as the root mean square error (RMSE).

Land Cover

Key land cover attributes, totalling eight main cover classes, were identified. These cover classes included vegetation (i.e. herbaceous saltmarsh, succulent saltmarsh, *Ceriops* spp., other mangroves (“Mangroves”), and woodland/grass terrestrial), main channel, artificial structures, and unvegetated flats (mudflat/saltpan). Land cover classes were identified with the orthomosaic generated from UAV-SfM to specify Manning’s roughness coefficient. Multiple attempts were made to classify the orthomosaic using unsupervised and supervised object-based image classification algorithms in ArcGIS Pro, but the results were deemed unreliable. A manual classification was performed using the drawing tools in ArcPro and assisted with field data (GPS points and photography). To achieve this, the entire orthomosaic was zoomed in so that each land cover feature could be circled around to create polygons of each land cover category. The polygons were then merged into individual land cover categories. The final land cover shapefile was made by assigning the entire study site as a mudflat/saltpan polygon (the dominant land cover). Each land cover shapefile was then erased to the mudflat/saltpan polygon in their order of overlapping in the field and then merged to create the final land cover map (Fig. S1). The manual classification did not allow the uses of a confusion matrix to provide an accuracy assessment. Nevertheless, the very high-resolution of the UAV-SfM imagery together with expert knowledge of the site coupled and on-ground imagery allowed confident reliability of the classification of land cover (Fig. 3).

Tidal Time Series

Tidal data were sourced from the Cape Ferguson tidal gauge (−19.277208; 147.060908), which is the nearest (3.5 km northeast) tidal gauge (Fig. 1a). To convert observed tidal heights to orthometric height in Australian Height Datum (AHD), the tidal datum for tidal observations at Cape Ferguson, which is 1.59 m (Bureau of Meteorology 2021), was subtracted from the observed tidal height. Tidal data at 10-min intervals was extracted from the 1-min interval dataset over a ~10-day period in January, June, and August (Table 2).

Validation Data

Water Level by Loggers

Water levels were monitored from November 2020 to March 2022 using pressure loggers (HOBO Water Level

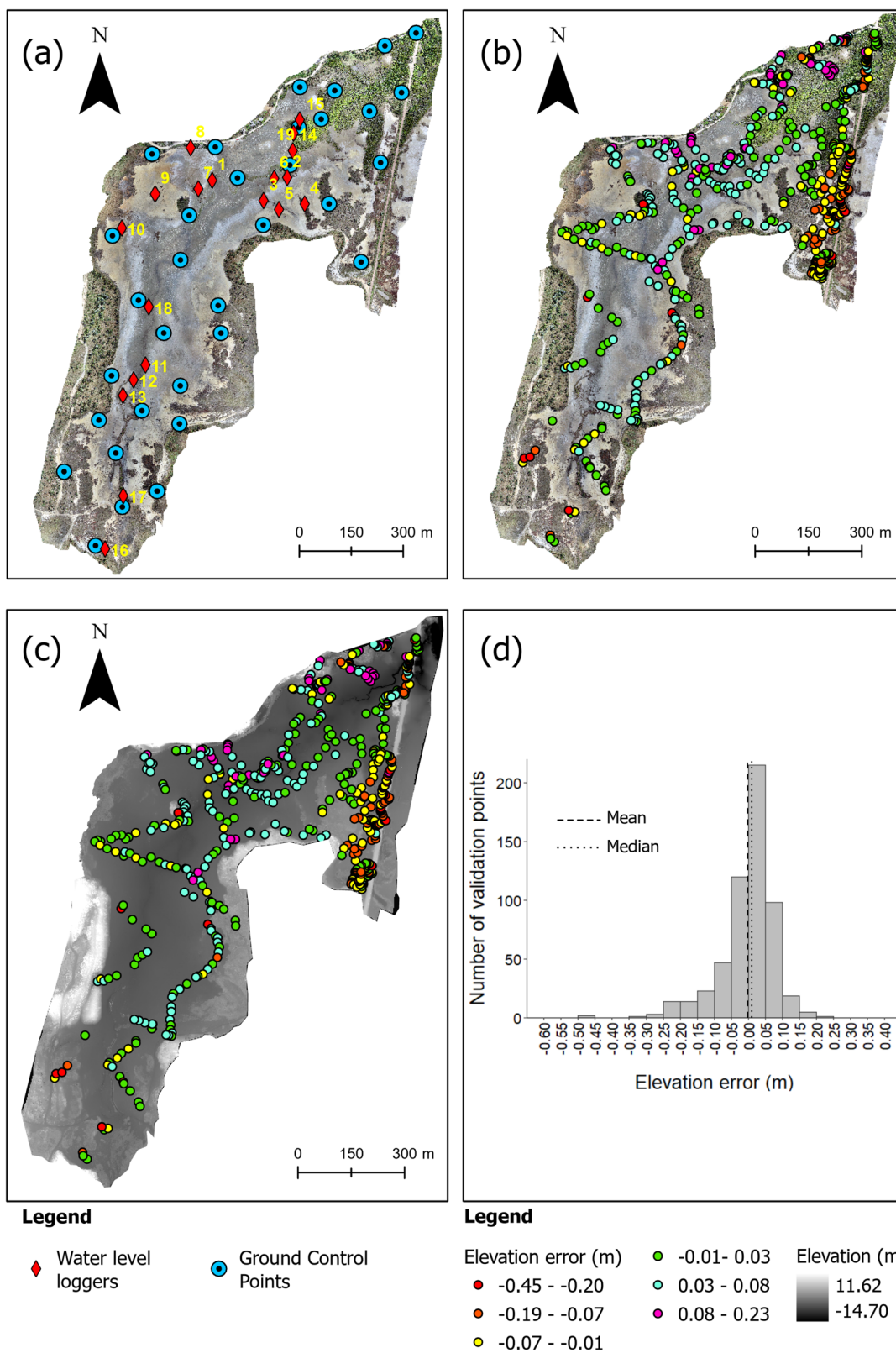


Fig. 2 **a** UAV-derived topographic map and DEM showing loggers and ground control points position; **b** validation points colour coded according to elevation error on the topographic map; **c** and on the

DEM; and **d** and graph of the distribution of elevation error of validation points (Software used: ArcGIS PRO)

Table 1 Workflow and parameters used to process the unoccupied aerial vehicle (UAV) imagery in Agisoft Metashape

<i>Process</i>	<i>Description</i>
1. Convert geographic coordinates and camera reference setting	Convert the coordinate systems and camera reference setting to the coordinate system of the GCPs surveyed with the RTK-GPS (i.e. from WGS84 to GDA2020/MGA zone 55 and AHD) using the “Convert” tool
2. Align image, generate sparse point cloud, and detect markers	Align photos using: <ul style="list-style-type: none"> • “High” accuracy • Select generic preselection and reference preselection • Set key point limit at 40,000 and tie point limit at 10,000 • Apply masks to none • Uncheck “Exclude stationary tie points”; guided “Image matching”: and “Adaptive camera model fitting”
3. Detect markers	Using the “Detect Markers” tool
4. Import GCPs	Import GCPs coordinates from CSV file <ul style="list-style-type: none"> • Set marker accuracy at 0.002 m • Adjust markers on image when necessary
5. Uncheck cameras and check all markers	Uncheck all cameras to force to optimisation process to use the markers surveyed using the RTK-GPS
6. Spare point cloud cleaning and optimisations	Using the gradual selection tool to delete the selected points: <ul style="list-style-type: none"> • Reckon uncertainty (level 15) and optimise (default parameters: f, cx, cy, k1-k3, p1, p2, no adaptative camera model fitting) • Reprojection error (level 0.4) and optimise • Reprojection error (level 0.3) and optimise • Projection accuracy (level 30) and optimise
7. Build dense cloud	Build dense point cloud using “High” accuracy and “Mild” depth filtering. Density of dense cloud = 4.81 points/m ²
8. Build orthomosaic	
9. Build DSM	
10. Build DEM	Use “Classify Ground Control Point” with parameters set at default

Data Logger (30-m U20L Series)) (Onset Compute Corp.) deployed over the study site (Fig. 2a). The loggers were rotated to new locations based on wetland terrain characteristics every 3 to 4 months due to a low number of loggers available at any time (4–8 loggers). This practice evaluated model performance across the entire study site to maximise spatial and temporal representation of water levels (Johnson and Pattiaratchi 2004). A logger was placed in a tree in the study area, approximately 1.5 m above ground, to log barometric pressure to compensate recorded pressure by the loggers (the logger remained in the same location for the entire study). The software onset HOBOWare Pro was used to convert pressure to water depth, which is calculated using fluid density (saltwater), reference water level (measured at the time of the logger deployment), and barometric pressure data.

Inundation by Sentinel-2

The second validation method consisted of comparing satellite imagery to compare observed and simulated inundation extent (Reid et al. 2014; González et al. 2023). Sentinel-2 imagery was downloaded from Planet Labs PBC 2022. As it was not possible to determine whether

the inundated area occurred by a preceding tide or was inundated on the satellite imagery, we opted to compare the maximum inundation extent for each simulation period to the first satellite imagery available following the highest tide of the simulation. In January, satellite imagery was taken 4 days after the highest tide (1/13/2021 at 09:20), with corresponding imagery taken the 21/01/2021 at 09:54. In June and August, the highest tide occurred at night (25/06/2021 at 01:20 and 21/08/2021 at 20:10, respectively). Imagery was only available 2 days after the highest tide in June (27/06/2021 at 10:00) and 3 days after the highest tide in August (23/08/2021 at 09:44).

Model Calibration and Validation

The hydrodynamic model was built and calibrated by simulating tidal dynamics over the ~10-day period in January, June, and August (Table 2), representing different logger positions. A central focus of the analysis was to simulate days representing a neap to spring tidal cycle (Table 2), with similar starting and ending tidal elevation across the simulations. Although temporal variations in saltmarsh morphodynamics have been described elsewhere (Sun et al. 2018; Jin et al. 2022) (e.g. 0–10 cm increase in soil elevation within











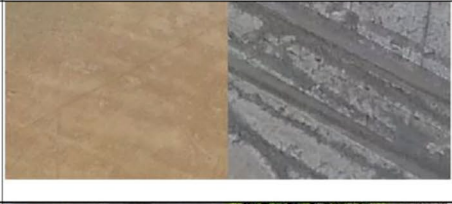
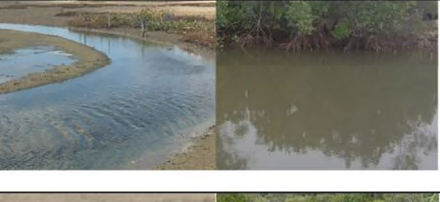



Land Cover Class	Example of Field Image	UAV-SfM
Succulent saltmarsh		
Herbaceous saltmarsh		
Mangroves		
<i>Ceriops</i> spp.		
Woodland Grass Terrestrial		
Mudflat/Saltpan		
Main Channel		
Manmade		

Fig. 3 Land cover class identified in the field for classification and corresponding examples viewed from the orthomosaic map derived from UAV-SfM

Table 2 Information on the three simulations computed to calibrate and validate the hydrodynamic model. Simulation starting elevation refers to the elevation at which the tidal level was at the beginning of

the simulation. Associated loggers used for calibration and validation are also shown (their position can be cross-checked with Fig. 1b)

Simulation	Start time	End time	Maximum tide elevation (m, AHD)	Simulation starting elevation	Loggers
January	07/01/2021, 14:00	17/01/2021, 07:10	2.07	0.54	1; 2; 3; 4; 5; 6; 7
June	18/06/2021, 01:20	30/06/2021, 07:30	1.96	0.55	8; 9; 10; 11; 12; 13; 14; 15
August	17/08/2021, 15:00	28/08/2021, 14:50	1.96	0.57	16; 17; 18; 19

6 months following months with higher inundation frequencies in *Spartina alterniflora* saltmarshes, Jin et al. 2022), it was assumed here that the site seasonal variability in morphodynamics was negligible across the simulation period, and the same DEM was used for all simulations.

The Manning's roughness coefficient is the principal calibration target in 2D HEC-RAS (Muñoz et al. 2021). Modeling performance was first assessed with an overall Manning's roughness coefficient of 0.025–0.035, which are the values recommended in the 2D HEC-RAS manual for bare land with minimal impediment on flow. At that stage, model parameters, including the theta implicit weighting factor, were adjusted (Table 3). The theta value is a weighting factor involved in the solving of the shallow water equations and is responsible for increasing model stability and output accuracy (Hicks and Peacock 2005). The theta value was reduced from 1 to 0.6 to improve model stability and better represent tidal wave propagation (Pasquier et al. 2019). The model was then manually calibrated by adjusting the

Manning's roughness coefficient of each land cover class (Table 4) starting with initial values suggested in the 2D HEC-RAS manual for similar cover classes and rising and adjusting the values until the simulated water level visually best matched the observed water levels. For instance, the 2D HEC-RAS manual recommends range values of 0.023–0.03 for barren land; 0.03 was used here for the mudflat/saltpan category. Similarly, the range of values suggested for emergent herbaceous wetland (0.05–0.085) was used as a basis to calibrate the values of herbaceous (*S. virginicus*) and succulent saltmarsh (*S. quinqueflora*). The friction values are considered in the middle to upper range of the suggested values from 2D HEC-RAS manual to compensate DEM and bathymetric errors (Mardani et al. 2020). Examples of model performance with constant Manning's and with the manual adjustments are found in the supplementary materials (Fig. S3).

After trial simulations to calibrate the model by modifying Manning's roughness coefficient and model parameters,

Table 3 Parameters used for the final calibrated 2D hydrodynamic model in HEC-RAS 6.1

Computation settings (2D flow)	Value
Theta	0.6
Theta warm-up	0.6
Water surface tolerance	0.003 (default)
Volume tolerance	0.003 (default)
Maximum iterations	20 (default)
Equation set	Diffusion wave
Initial conditions ramp up fraction	(Default)
Number of time slices	1 (default)
Computation time step base	1 min
Base output interval	10 min
Hydrograph output interval	10 min
Mapping output interval	10 min
<i>2D flow area</i>	
Points spacing (m)	2×2 m (smaller cell size did not improved the model but significantly increased processing times)
Default Manning's value	0.035

Table 4 Manning’s *n* roughness coefficient used in the validated model based on the range of the recommended values by the HEC-RAS manual

Land cover	Manning’s <i>n</i>
Mudflat/saltpan	0.03
Woodland grass terrestrial	0.04
Herbaceous saltmarsh	0.06
Succulent saltmarsh	0.05
<i>Ceriops</i> spp.	0.08
Other mangroves (<i>Avicennia</i> spp. and <i>Rhizophora</i> spp.)	0.08
Manmade (gravel and concrete roads)	0.1
Main channel	0.035

we observed a consistent offset of 0.3–0.4 m between observed and simulated water levels. We attributed that to a site-specific offset in datums (likely due the distance to tidal gauge used to parameterise the model) and uncertainties in the DEM (including bathymetry, notably in the area where the mangrove forest was removed, and the channel was reconstructed) (see Discussion for details on DEM sources of inaccuracies) and subtracted 0.35 m to observed tidal data. Note that the above description of the calibration of the Manning coefficients to obtain the final Manning values was carried out after correction for the offset.

The model was validated by comparing the depth recorded by the loggers and the depth simulated by the model. Differences between the maximum observed and predicted depth are presented for each logger, together with RMSE of maximum depth error and R^2 . RMSE and R^2 between observed and simulated water depths are also presented. RMSE and R^2 of inundation duration were computed by calculating the number of 10-min time step being greater than 0 m for both the depth recorded by the loggers and the depth simulated by the model. The number was then multiplied by 10 and converted to hours. The extent of inundation was further validated by comparing the inundation boundary from satellite imagery (Sentinel-2 at 3-m resolution) to the simulated boundary.

Table 5 Assessment of elevation error between RTK-GPS validation points and UAV-DEM elevation. Positive mean values indicate elevation underestimation, while negative mean values indicate elevation overestimation

	Land cover	<i>n</i>	RMSE (m)	Mean (m)	SD (m)	SE (m)
	<i>Whole DEM</i>	562	0.081	–0.002	0.081	0.003
Unvegetated	Mudflat/saltpan	357	0.054	0.022	0.050	0.003
Vegetated	Succulent s	76	0.078	–0.008	0.078	0.009
Vegetated	Herbaceous s	59	0.123	–0.081	0.096	0.011
Vegetated	<i>Ceriops</i> spp.	4	0.080	0.059	0.060	0.031
Vegetated	Mangroves	2	0.041	–0.013	0.055	0.039
Vegetated	Grass/wood	46	0.155	–0.088	0.128	0.019
Water	Main channel	5	0.107	–0.058	0.101	0.045
Manmade	Manmade	13	0.064	–0.011	0.058	0.016

Results

DEM Generation and Accuracy Assessment

The UAV-SfM generated a 3-cm resolution DEM (Fig. 2), with a RMSE in elevation of 8 cm (Table 5). The distribution of elevation error is leptokurtic, with some outliers in vegetated areas (Fig. 2d). Elevation tended to be overestimated in vegetated areas (Table 5). RMSE in elevation was higher in vegetated wetlands (4 cm in mangroves to 12 cm in herbaceous saltmarsh) compared to unvegetated areas (mudflat/saltpan RMSE = 5 cm) (Table 5). The lower elevation error in the mangroves compared to herbaceous saltmarsh is likely because only two successful validation points were surveyed with the RTK-GPS in the mangrove forests (Table 5). This made it difficult to assess DEM errors for the mangrove land cover.

The Hydrodynamic Model

Overall, simulated water levels and timing fitted the observed water levels ($R^2 = 0.51$ to 0.71 and RMSE = 0 to 0.05 m) (Fig. 4a). This gives confidence that the model performed well in predicting water level and inundation across the study site. Simulated maximum depth at each logger point was close to that observed, with an RMSE of maximum depth of 0.07 m and a correlation coefficient R^2 of 0.93 (Fig. 4b). RMSE between observed and simulated depth ranged from 0 m (loggers 9, 10, 16, 4—in areas that remained dry during the study period) to 0.053 m. Correlation coefficients indicate moderate to strong correlation (0.506 – 0.712) between simulated depth and observed depth, with the exception at logger 17 where R^2 was 0.24 (Fig. 4a). Some specific exceptions in model performance in simulating depth are noticeable, notably at loggers 2, 3, and 14, where simulated maximum depth was greater than 9 cm of the observed depth. At logger 2, which was positioned adjacent to the mangrove channel, the difference between maximum simulated and observed depth was 0.19 m—the

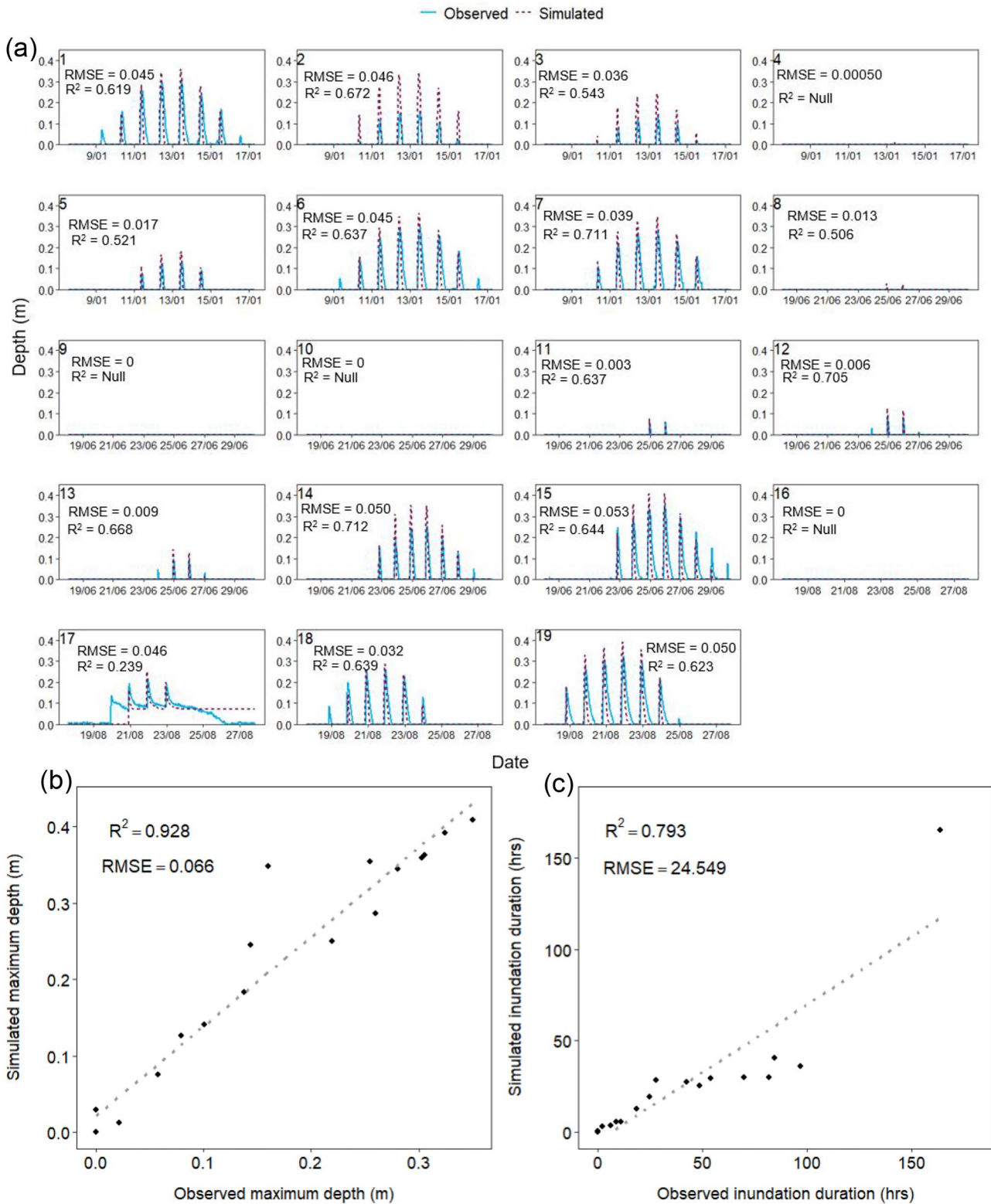


Fig. 4 a Simulated depth over recorded depth (HOB0 water level logger) at each logger position with root-mean-square error (RMSE) and correlation coefficient (R^2); b distribution of maximum observed

and simulated depth (for all simulations) with R^2 and RMSE; c distribution of observed and simulated inundation duration in hours with R^2 and RMSE (Software used: Rstudio, Word)

highest recorded. Without this outlier, the RMSE was 0.05 m and the correlation coefficient R^2 was 0.98. In addition, the model simulates a constant water level following inundation at logger 17, a logger placed in the isolated channel at the southern part of the study site. When pooling all loggers, simulated inundation durations were lower than observed inundation durations with a R^2 of 0.79 and a RMSE of 24.55 h (Fig. 4c). The large RMSE in inundation duration was largely driven by the underestimation of inundation duration in the main channel at loggers 1, 6, 15, 18, 19, and a small drain at logger 7. Without these six loggers, the RMSE dropped considerably, reaching 5.09 h and a R^2 of 0.99. Model performance was also notably reduced as simulated arrival time and maximum water level tended to be 10–60 min earlier than observed. When adjusting for this delay, overall model performance improved in most logger emplacements ($R^2 > 0.789$) (Table S1). For instance, if simulated inundation had arrived 60 min later at logger 2, the R^2 would have increased from 0.672 to 0.946 (Table S1).

Comparisons between satellite imagery and simulated inundation extent for each of the three simulation periods (Fig. 5) support that the model accurately modelled tidal inundation. In January, observed inundation extent was 49.82 ha compared to the simulated extent of 53.02 ha. In June, observed and simulated inundation extents were respectively 41.13 ha and 43.07 ha, while in August, it was 43.20 ha (observed) and 42.89 ha (simulated).

Hydroperiod

The model developed here indicated that a tidal height of near 2.95 m (1.36-m elevation AHD) is required to start inundating the wetland above the mangrove-marsh ecotone

(i.e. saltmarshes and saltpan) in the study area upstream of the culvert. In addition, the higher tides observed in January (0.2 m higher compared to June and August) resulted in an increased inundation extent of 10 ha of tidal wetland (Fig. 6).

Maximum inundation depth across most of the study site and simulation periods remained shallow at < 0.4 m (Fig. 6). Specifically, 68.2%, 82.5%, and 83.5% of the total inundation extent for the January, June, and August, respectively; simulations had a maximum depth of less than 0.4 m. Inundation frequency is low across most of the tidal wetland (Fig. 6). More specifically, in all simulations (January, June, and August), more than 50% of the maximum tidal boundary was inundated less than 23.3, 29.4, and 26.4 h, respectively (Table 6). Only the defined mangrove channel areas remain inundated 80–100% of the simulation period (Fig. 6).

Discussion

Low-lying tidal wetlands are at threat owing to changes in tidal inundation due to sea-level rise and anthropogenic disturbances giving rise to the urgent need to develop modelling tools for managers to better implement coastal management and restoration planning decisions. This study presents a workflow that can be used by managers to develop a relatively simple 2D hydrodynamic model, computed using freely available software (HEC-RAS) that requires minimal data inputs (UAV-SfM-derived DEM and land cover, and water level data). The resolution and accuracy presented here make this approach particularly useful for managers challenged with working in low-relief coastal wetlands where centimetre-scale changes in topography are the difference between water connection and not.

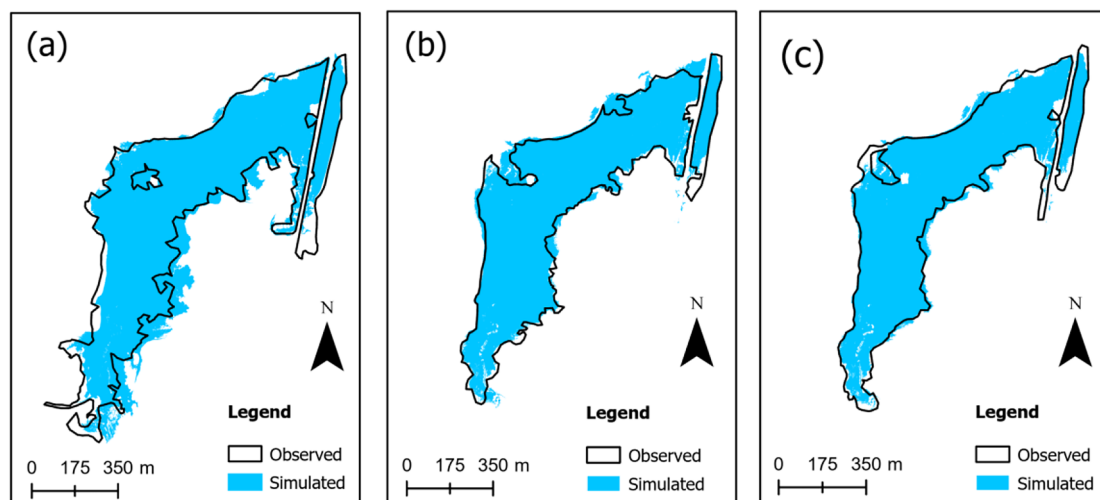


Fig. 5 Comparison of simulated and observed (Sentinel-2 imagery) inundation boundaries for (a) January, (b) June, and (c) August simulations (Software used: ArcGIS Pro)

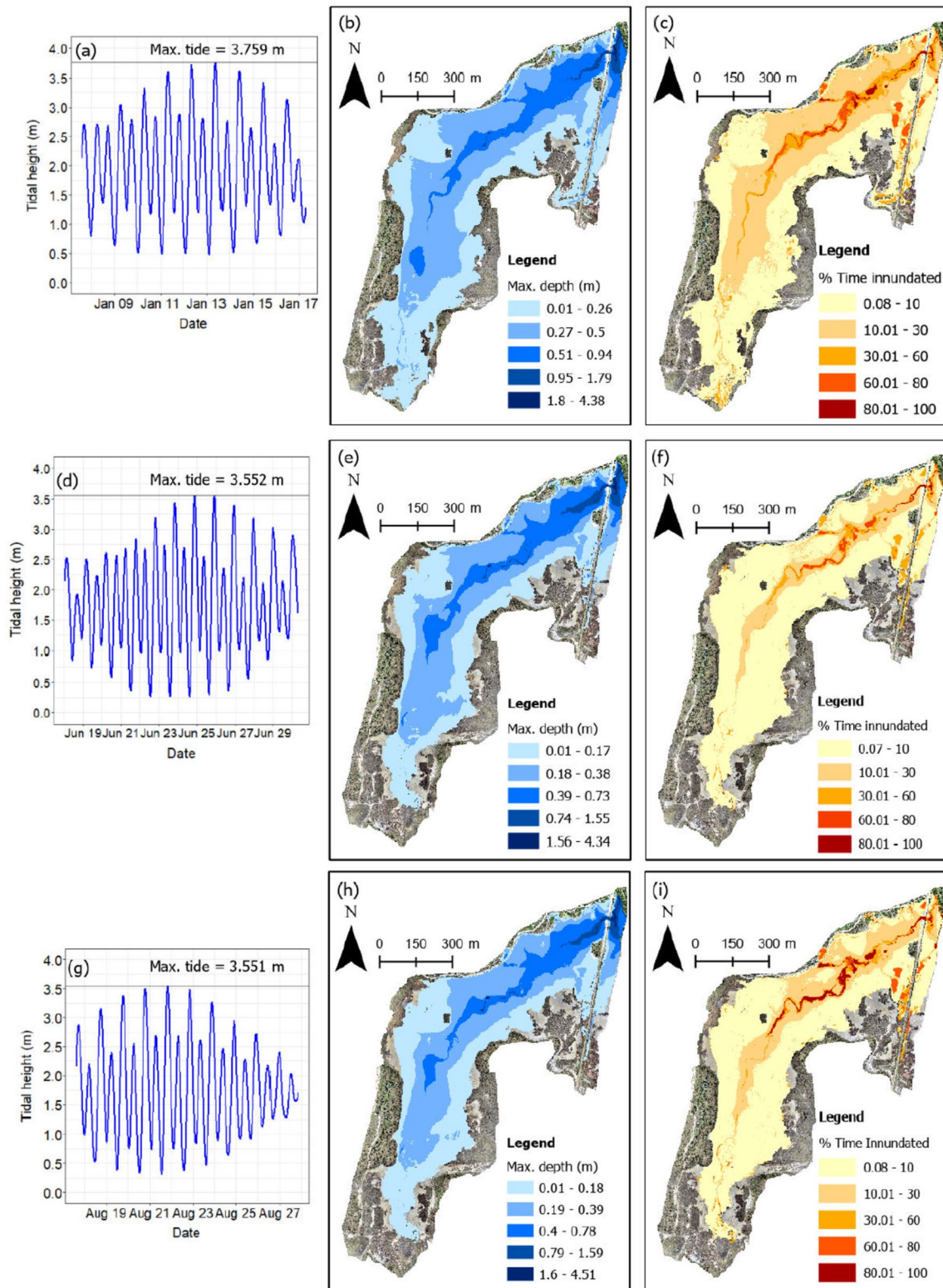


Fig. 6 Examples outputs for each simulation. Observed tidal height for January, June, and August (a, d, g), respectively, recorded at Cape Ferguson tidal gauge ($-19.277208; 147.060908$), Australia and cor-

responding spatial distribution of maximum depth (b, e, f) and percentage of time of inundation (c, f, i) (Software used: ArcGIS Pro; RStudio)

The Importance of High-Resolution Topographic Data in Coastal Studies

The model presented here illustrates how small changes in topography (e.g. vehicle tracks) can interfere with surface hydrology in shallow water environment (Fig. 7). For instance, a 20-cm increase in tidal height was related to a 10-ha increase in upper tidal areas being inundated. This suggests that even minor alterations in tidal inundation due to anthropogenic activities (e.g. culverts and tidal gate; Kroon and Phillips 2015) or sea-level rise might affect the extent of intertidal wetland (e.g. saltmarshes) inundation.

Vehicle uses on saltmarshes has been shown to cause direct saltmarsh degradation and disappearance (Trave and Sheaves 2014; Blakely et al. 2022). In this study, vehicle tracks through the wetlands were found to influence tidal inundation pathways and create unnatural flow paths that remain wet. The present observations support the model that vehicle uses on saltmarshes might affect tidal wetland hydrological connectivity and potentially interfere with eco-hydrological processes at the local scale. For instance, constant inundation might affect soil properties (e.g. water content, salinity, compactness) and in turn vegetation distribution and soil suitability to burrowing organisms (Trave and Sheaves 2014). In light of these findings and in line with several other studies (Hannaford and Resh 1999; Kelleway 2006), coastal management authorities must carefully consider whether these activities should occur in such sensitive ecosystems. These observations also support the importance of utilising fine resolution DEMs (Annis et al. 2020), where employing a coarser DEM resolution (e.g. 1 m) would not have detected road

tracks and small channels that would seemingly influence inundation (Fig. 8).

Fig. 7 **a** Orthomosaic map of 0.02-m resolution and **b** associated 0.03-m digital elevation model (DEM) (this study) generated from UAV-SfM. **c–f** Examples of the effects of DEM resolution on the representation of topographic features are shown. **c** The same area (black rectangle in **a** and **b**) is represented by a 5-m DEM derived from LiDAR (Geoscience Australia); **d** 1-m DEM derived from LiDAR (QLD Government; and **e** 0.03 m DEM derived from UAV-SfM (this study). **f** The effects of microtopographic features represented by the 0.03-m UAV SfM on tidal flow trajectory and depth are shown, where tidal inundation simulated by the 2D hydrodynamic model developed in this study is overlaid on the orthomosaic map (Software used: ArcGIS Pro; RStudio)

tracks and small channels that would seemingly influence inundation (Fig. 8).

Key Considerations for Hydrodynamic Modelling of Tidal Wetlands

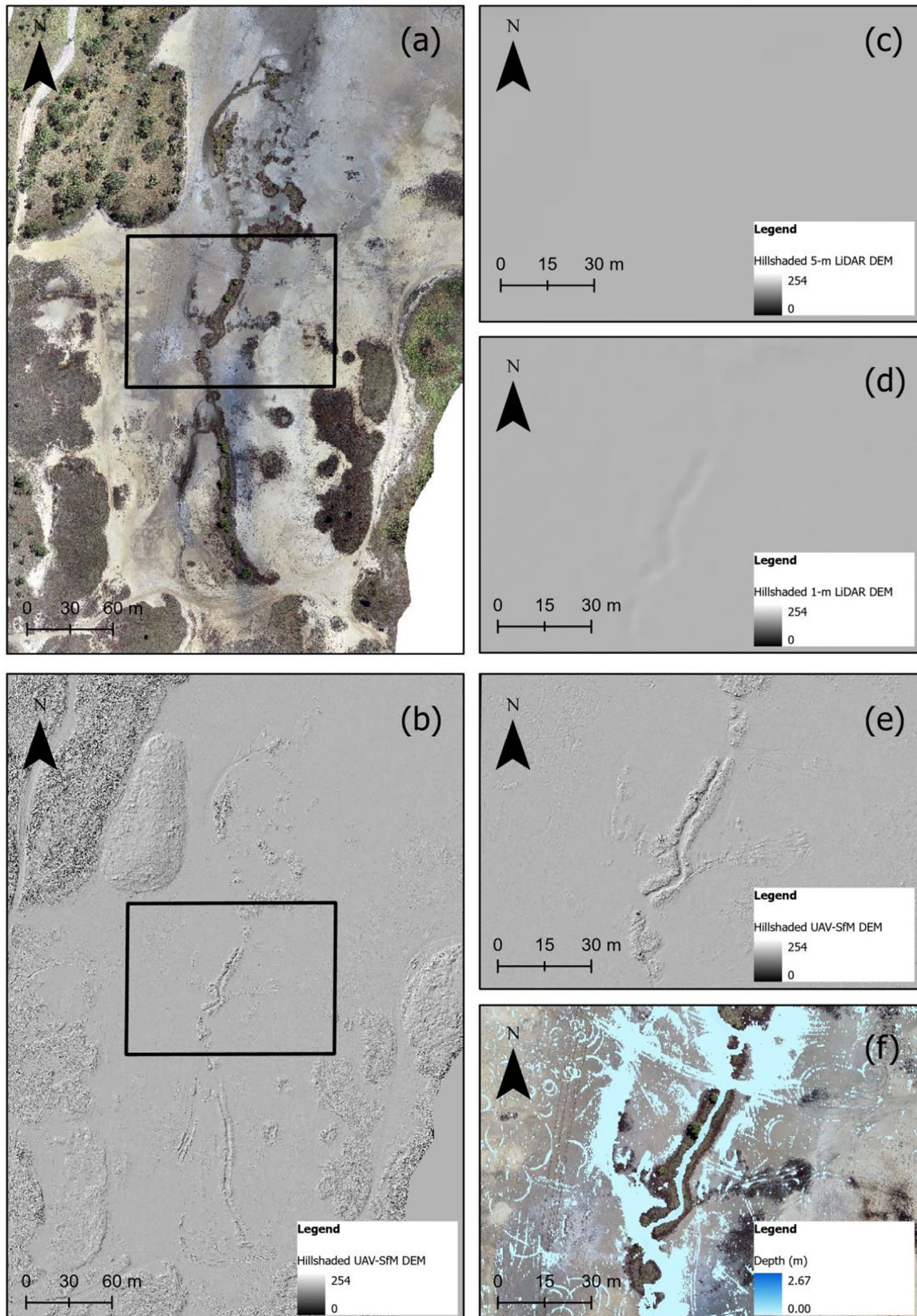
Choice of Model

With an RMSE error between maximum observed and simulated depth of 7 cm and similar trends between simulated and observed depth, the present model was considered a reliable tool to understand tidal wetland hydroperiod. The largest difference between the maximum observed and simulated depth (19 cm) is also lower than reported in other coastal flooding studies (e.g. 33 cm in Kumbier et al. 2022). Correlation coefficients between observed and simulated depths were nevertheless lower than reported in another hydrodynamic study of a tidal wetland complex composed of similar saltmarshes and mangroves species ($R^2 = 0.98–0.99$, Kumbier et al. 2022).

Table 6 Maximum (max.) observed tidal height for each simulation and associated maximum simulated tidal extent area (ha). The percentage of the area inundated for a given number of hours (expressed

in brackets) is also shown. The number of hours represents <10%, 10–30%, 30–60%, 60–80%, and 80–100% of time of each simulation

	January 2021	June 2021	August 2021
Max. tidal height (m)	3.76	3.55	3.55
Max. inundation extent (ha)	52.95	43.01	42.84
Simulation time (hours)	233.17	294.17	264.00
Percentage of area inundated less than 10% of simulation time (h)	50.98% (<23.32 h)	76.15% (<29.42 h)	68.47%(<26.40 h)
Percentage of area inundated between 10 and 30% of simulation time (h)	36.40% (23.32–46.63 h)	15.29% (29.42–88.25 h)	22.34% (26.40–79.20 h)
Percentage of area inundated between 30 and 60% of simulation time (h)	6.47% (69.95–139.90 h)	5.07% (88.25–176.50 h)	2.78% (79.20–158.40 h)
Percentage of area inundated between 60 and 80% of simulation time (h)	4.54% (139.90–186.53 h)	2.59% (176.50–235.33 h)	2.45% (158.40–211.20 h)
Percentage of area inundated between 80 and 100% of simulation time (h)	1.29% (186.53–233.17 h)	0.38% (235.33–294.17 h)	3.50% (211.20–264.00 h)



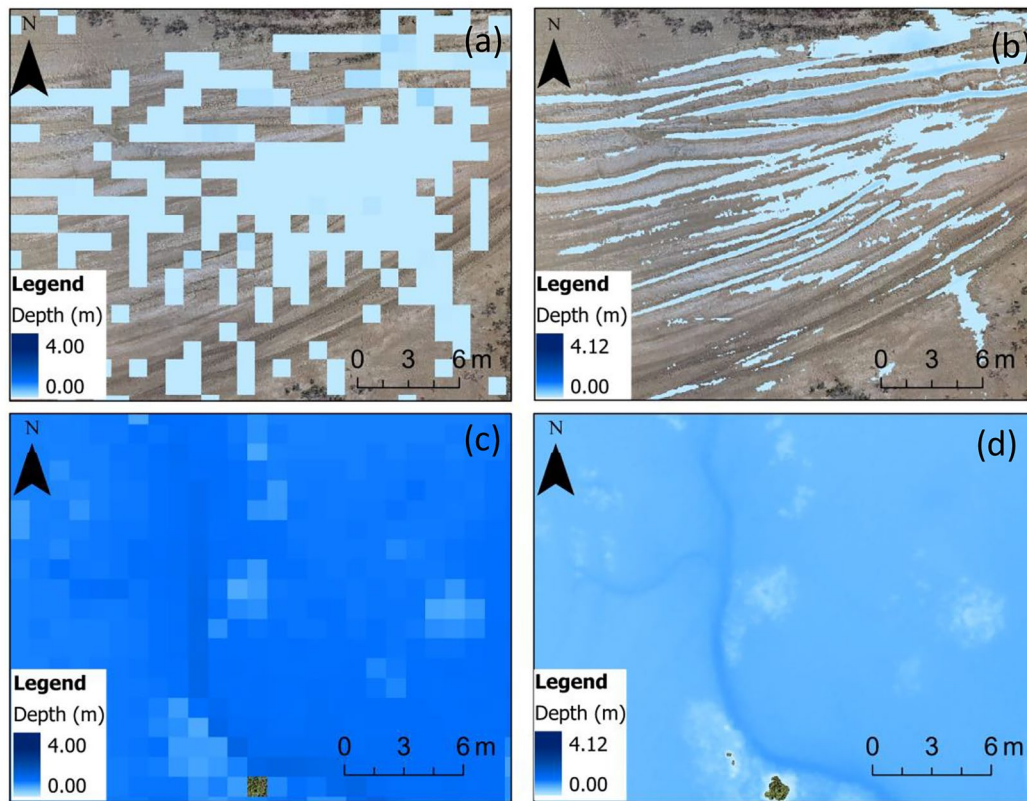


Fig. 8 Comparisons between the hydrodynamic modelling outputs based on the DEM derived from UAV-SfM resampled at 1-m resolution (**a, c**) and the 0.03-m UAV-SfM (**b, d**) showing depth overlaid on the orthomosaic map (Software used: ArcGIS Pro)

Spatial variability in model performance was observed, notably near the mangrove channel, where simulated depths were higher than recorded depth (notably at loggers 2, 3, and 14). Previous studies have attributed spatial variability in hydrodynamic model performance to model configuration and uncertainty in inputs data (e.g. DEM, mesh structure, grid size, spatial variability in roughness, boundary condition, and processing parameters) (Ganju et al. 2016; Anees et al. 2017). For instance, it is possible that a combination of DEM inaccuracies and the fact that the tidal gauge was placed outside of the study area could have resulted in the observed difference of 0.3–0.4 m in water depth during calibrations and resulted in the need to subtract 0.35 m to the tidal data. The use of the unsteady flow equation (UFE) instead of the shallow water equation (SWE) that considers local and advection acceleration might also have decreased water depth accuracy (Yilmaz et al. 2023) and led to the need to correct the 0.3–0.4 m offset. Solving the UFE instead of the SWE might also have led to the shortened arrival time as the UFE tends to simulate higher flow velocities (Marangoz and Anilan 2022), although slower propagation has also been described with UFE (Martins et al. 2017). DEM (including bathymetry) inaccuracies could also have led to the higher

simulated depths and shorter simulated inundation compared to the loggers placed in the mangrove channel as well as the overall earlier simulated arrival times. Manning's n values are the only parameter that needs to be adjusted in HEC-RAS and seemed not to importantly influence arrival time in the present study (Fig. S3). Hence, it is more likely that other choices (DEM and boundary condition) led to the lower performance in the model near the mangrove channel and in arrival times. A detailed sensitivity analysis and calibrations of the model are essential to understand the effects of model configuration and/or uncertainty in input data on model performance (Hall et al. 2009). Detailed sensitivity analyses were not conducted in the present study but might have improved the assessment and calibration of the model (Pan et al. 2011).

Eco-hydrological processes such as variability in soil characteristics (e.g. stratigraphy and chemistry), groundwater dynamics (e.g. Wilson and Morris 2012), or macropores (Xin et al. 2009) can also influence surface and sub-water flow interactions, and thereby the spatio-temporal variability of tidal wetland inundation. Monthly variability in tidal inundation frequency and sediment availability can also lead to seasonal changes in soil elevation (Jin et al. 2022). For

instance, a 0–10 cm increase in soil elevation was reported in *S. alterniflora* saltmarshes (Jin et al. 2022). The increase occurred over a 6-month period following months with higher inundation frequencies. These processes might have caused some of the differences between observed and simulated water depth, notably near draining channels and vegetated areas as bare flats are less prone to seasonal changes in soil elevation (Jin et al. 2022).

Dynamic mechanistic numerical models (e.g. ecogeomorphic models) that take into account hydrology and soil morphology (e.g. Marois and Stecher 2020) and feedback processes between ecology and hydrogeomorphology (e.g. Alizad et al. 2016) may better represent small-scale processes that influence tidal wetland hydrology.

Similarly, adding rainfall, barometric, evapotranspiration, and wind data to the present 2D hydrodynamic model could enhance model applicability in wider meteorological contexts (Karim et al. 2021). For instance, evapotranspiration is important in dry areas (Wallace et al. 2015) particularly when the model is ran for longer periods such as months or years. In our case, there will be negligible evapotranspiration in a 10-day model run. However, evapotranspiration might have caused the different pattern in observed and simulated depth at logger 17, which was placed in a depression. Simulated depth remains constant following inundation, while observed depth decreased over time. Adding evapotranspiration data could therefore increase model accuracy in those areas characterised by more complex topography.

The selected model must represent the dominant processes of the study site, which means that end-users of these approaches must, therefore, be careful and understand the selected model's limitations, such as error and uncertainty (Wechsler 2007), and is within an acceptable limit to answer ecological questions. Based on the objectives of the simulation, different models are selected, and processes need to be added or deleted from the model. For example, groundwater/surface water interaction cannot be modelled in all 2D models. We believe that the approach presented provides a way forward in understanding tidal wetland inundation where there is limited starting data.

UAV-Derived DEM

The approach to UAV data collection, image processing, and post-processing implemented in this study derived DEMs with a resolution of 3 cm and high accuracy (8-cm elevation error) suitable for small-scale and detailed hydrodynamic modelling tidal wetlands. The DEM accuracy assessment results are similar to that of studies that have used SfM to derive DEMs, where DEM RMSE range from 3 to 8 cm (e.g. Gonçalves and Henriques 2015; Koci et al. 2017; Taddia et al. 2021).

Although studies have developed high resolution UAV-SfM-derived DEMs and highlighted their potential uses in water management (Kalacska et al. 2017; Taddia et al. 2021), only a few studies have used UAV-SfM-derived DEMs to parametrise 2D hydrodynamic models (Tamminga et al. 2015; Yalcin 2018; Annis et al. 2020; Li et al. 2021). To the best of our knowledge, the present study is the first to use a UAV-SfM-derived DEM to parametrise a 2D hydrodynamic model of a tidal wetland. Although, UAV-SfM presents advantages to create DEM for the management of tidal wetlands (Table 7), the key limitations encountered in the present study remain the same as that of floodplain and rivers, which are attaining ground points in vegetated areas (e.g. Hashemi-Beni et al. 2018), obtaining bathymetric data (Tamminga et al. 2015), and limitations due to GCPs requirements and computing demand.

The elevation errors computed in this study are less, near, or higher than those of similar tidal wetland studied with UAV- or LiDAR-DEM. For instance, the UAV-DEM-derived by Taddia et al. (2021) (which was not further cleaned after Agisoft Metashape ground-point classification) obtained a RMSE of elevation of 1.5 cm for mudflats from UAV-DEMs, which is coarser to the 5 cm obtained in this study. Their RMSE for saltmarshes (dominated by *Spartina alterniflora*) was 20 cm (compared to 8–12 cm in the present study), which was considered too coarse by the authors to investigate geomorphological changes. Hladik and Alber (2012) obtained a RMSE of 5 cm for *Salicornia virginica* (corrected Lidar-DEM), similar to the RMSE of 8 cm obtained here for succulent saltmarshes dominated by *S. quinquefolia*. Herbaceous saltmarsh elevation errors (dominated by *S. virginicus*, with *C. dactylon* and *Juncus* spp.) were also comparable, although higher (12 cm), to the RMSE of low and medium *S. alterniflora* (5–7 cm) (Fernandez-Nunez et al. 2017) and *Juncus roemarianus* (10 cm) (Hladik and Alber 2012) derived from corrected Lidar-DEMs.

The performance of in-built ground point filtering algorithms (e.g. geometric algorithms such as the progressive morphological filter (PMF)) available in photogrammetric software remains poor in highly vegetated areas such as herbaceous saltmarsh (Štroner et al. 2021). Studies have attempted to address this by developing more specific algorithms to remove non-ground points such as in mangrove forests (e.g. Navarro et al. 2020; Mohamad et al. 2021). However, trade-offs between study site size (Navarro et al. 2020) and resolution (Mohamad et al. 2021) remains due to the high computing/processing demand when using those techniques. Those difficulties are overcome with Lidar-UAV (Pinton et al. 2020, 2021; Cao et al. 2021).

Here, the relatively simple approach used to create a DEM from a DSM (digital surface model) might not have been suitable if the site was a mangrove-dominated system with

Table 7 Summary of advantages and limitations of the present UAV-SfM and 2D hydrodynamic modelling workflow, as well as further research and improvements, alternatives, examples of applications, and key outcomes

	UAV-SfM for hydrodynamic modelling	HEC-RAS 2D modelling
Advantages	<ul style="list-style-type: none"> • High-resolution DEM (3 cm) • High-resolution (0.02 m) orthomosaic map that can be used for Manning's <i>n</i> roughness calibration and cover assessments (e.g. vegetation distribution, patch size, road tracks) • Instruments low-cost (<10,000) • User-friendly instruments and photogrammetric software • Practical licences not required for using light quadcopters in research in some countries (e.g. Australia, only a theoretical online test is required). 	<ul style="list-style-type: none"> • Free • User-friendly and highly documented • Highly dependent on DEM resolution and accuracy • Many mapping outputs options are available • Official tidal gauge data can be used as boundary condition. • Bathymetric, precipitation, and wind data can be added in a 2D grid system. • In-built tools to reconstruct channel structure and bathymetry.
Limitations	<ul style="list-style-type: none"> • Applications remain limited by vegetation and water. • Not easily applicable in dense mangrove forests or in low-tide terrain (e.g. seagrasses, mudflats). • Study site size needs to remain small (<100 ha) due to GCPs surveying, short UAV battery life, limited day times at which UAVs can be flown, and data storage, processing, and analyses, which require high computing demands. 	<ul style="list-style-type: none"> • Simulation processing times are principally controlled by computer processor speed. • Simulations might require higher computing demands than other 2D hydrodynamic modelling software such as Delft3D-FM (Muñoz et al. 2021) • Fixed grid modelling • Computational cells have a maximum of 8 sides.
Further research and improvements	<ul style="list-style-type: none"> • DEM accuracy in vegetated areas • Ground point classification algorithms • Workflows to reduce GPCs uses (e.g. Taddia et al. 2020) • UAV-borne topographic LiDAR and UAV-based green LiDAR system (GLS) (TDOOT GREEN 2022) for higher DEMs accuracies in vegetated and inundated areas • RTK-UAVs and/or PPK techniques to reduce GCPs (Taddia et al. 2020) • Multi-spectral UAVs for high-resolution mapping of vegetation (Yeo et al. 2020; Nardin et al. 2021) 	<ul style="list-style-type: none"> • 2D/3D modelling software (e.g. TUFLOW, MIKE 21, MIKE 3, Delft3D) for coastal and estuarine modelling that propose both unstructured or fixed structured grid modelling and in which many environmental variables can be added (Karim et al. 2021; Kumbier et al. 2022)
Alternatives for potentially higher performances at a higher financial cost		
Applications and uses for tidal ecosystems management	<ul style="list-style-type: none"> - Restoration and protection of hydrological connectivity - Identification of suitable restoration sites - Tidal vegetation replantation projects - High-resolution mapping of tidal wetland vegetation distribution - Evaluation of changes over time (e.g. vegetation loss/gain; elevation changes) - Modelling sea-level rise or reduction of tidal inundation and their effects on tidal wetland hydroperiod - Identification of local stressors (e.g. vehicle uses on saltmarshes) - Fish and invertebrate habitat management (e.g. nurseries) - Ecological processes related to hydroperiod (e.g. prey-pulses, food webs) - Identification of mosquito breeding sites 	<ul style="list-style-type: none"> • Quantitative and visual understanding of critical tidal wetland connectivity with minimal expertise and financial resources • Impactful (i.e. visual and high-resolution) and understandable communication of results to stakeholders, practitioners, and investors. • Possibility to quantitatively link hydroperiod to tidal wetland ecological and morphological processes as well as human impacts.
Key outcomes		

dense vegetation. Indeed, this technique (Agisoft Metashape algorithm to remove non-ground points followed by manual cleaning of the mangrove forest using ArcGIS Pro) led to artefacts and uncertainties in the DEM in vegetated areas and below water (elevation error increases from -1 to 8 to 8 – 20 cm in some vegetated areas near the mangrove forest after DEM cleaning). This represents a weakness in the present approach as this area is a critical part of the study site where the system is flooded and drained. Yet uncertainties in the DEM in this area could not be explicitly addressed as the RTK-GPS did not work in the mangrove forest, and accessibility and safety due to crocodiles were impeded along and in the channel. This workflow would also not be suitable for terrain under low-tide level (e.g. seagrasses). In addition, manual classification of land cover makes this technique inappropriate for larger sites. The uses of multi-spectral UAVs for high-resolution mapping of vegetation with similar RGB colour would have helped in the classification of land cover here (Yeo et al. 2020; Nardin et al. 2021)—where complex overlaps of vegetation with similar characteristics (e.g. herbaceous saltmarsh and terrestrial grass; mudflat and succulent saltmarsh) rendered autonomous classification unreliable.

Model Validation

The limited availability or difficulty in acquiring accurate validation data is a recognised cause of uncertainty in hydrodynamic modelling studies (Molinari et al. 2017). We advise using water level loggers for validating hydrodynamic modelling results. Our water level loggers identified the need to offset the calculated simulated model depths from the observed water depths. Solely comparing simulated inundation extent to inundation extent extracted from Sentinel-2 imagery reinforced that the model was efficient at modelling tidal inundation extent, but would not be able to quantify this offset. Additionally, the satellite imagery resolution (3 m) was also markedly coarser than the resolution of UAV-SfM-derived DEM (0.03 m), making it challenging to distinguish the inundation boundary on the satellite imagery. Remotely sensed data from satellites are increasingly used to validate large-scale hydrodynamic modelling (Teng et al. 2017). We suggest, however, that in the context of high-resolution, small-scale hydrodynamic modelling such as presented here, on-ground data (e.g. water level loggers) should be collected when possible and used in conjunction with other validation methods (e.g. remotely sensed data, Reid et al. (2014)).

Applications, Hydroperiod, and Future Studies

The model quantitatively shows what has been described non-empirically in the literature concerning that saltpan and saltmarsh inundation is infrequent ($< 10\%$ of simulation time) and

shallow (< 0.3 m) in Australia (Thomas and Connolly 2001). However, the model also highlights that maximum depth and duration of inundation can vary at small spatial (i.e. few centimetres) and temporal (e.g. minutes to lunar month) scales. Accounting for this will be essential for the management and restoration of coastal ecosystems (Sheaves et al. 2021). By showing that micro-topographic differences result in locally changing hydroperiod, the model highlights that these ecosystems are complex, with site-specific nuisances suggesting that even small human interventions such as vehicle uses could have the potential to modify their function as productive coastal habitat. For instance, waterlogged soil resulting from faults in soil elevation caused by vehicle uses promote *A. marina* growth, algal mats formation, and mosquito breeding sites, while considerably reducing saltmarsh habitability to invertebrate populations (Kelleway 2006).

The workflow presented here is particularly meaningful given increasing interest in restoring blue carbon ecosystems above low tide levels (Macreadie et al. 2021; Lovelock et al. 2022). Financial resources for the restoration and conservation of ecosystems are highly competitive and request measurable outcomes (Vanderklift et al. 2019; Waltham et al. 2021). Concurrently, the lack of quantitative understanding of tidal wetland functioning and hence of potential measurement of restoration success increases dubiety in investing in coastal restoration (Waltham et al. 2020). Achieving a spatial and quantitative understanding of tidal hydrological connectivity, such as provided by the simple workflow presented here, will provide cost–benefit solutions for investors and stakeholders to assist in predicting and measuring restoration and protection outcomes. Indeed, this workflow has many potential applications in tidal ecosystem management (Table 7). For instance, it can be used to quantify tidal hydrological connectivity, which can then be associated with information on elevation, tidal vegetation distribution and survival, accretion rates, and carbon storage capacity and how this might change with sea-level rise or reduction of tidal inundation. Such understanding is paramount in identifying, implementing, and evaluating the success of restoration and protection of blue carbon ecosystems. Repetitions of the same workflow overtime can also provide information on morphological evolution of tidal wetlands (Taddia et al. 2021).

Conclusion

New advances in remote sensing techniques and hydrodynamic modelling software are opening new horizons to understanding tidal wetland hydrodynamic at high spatio-temporal resolution. In this study, we present a case for using UAV-SfM to derive DEMs with a high resolution and accuracy suitable to parametrise small-scale hydrodynamic models of tidal wetlands. With some exceptions in model performance

in the mangrove channel, tidal inundation depth and duration were represented with acceptable accuracy between simulated maximum observed and simulated depth and duration of inundation. The DEM derived from UAV-SfM was accurate (7-cm RMSE) but still represented challenges in obtaining ground points in the mangrove forest and in the main channel, which likely caused lower model performance (higher depth and duration inundation error) in those areas. Overall, representation of tidal wetland inundation patterns was importantly improved by using the high-resolution 3-cm UAV-SfM DEM. The approach shows that small changes in elevation such as due to vehicles tracks and water level modify tidal wetland inundation patterns and hydrological connectivity at small temporal and spatial scales. These methods will assist in planning, defining, and implementing practical and measurable restoration and protection projects that consider tidal flooding dynamics and implications in areas with very low elevation. Calibrated hydrodynamic model also can be used to predict future inundation and hydrodynamic levels due to projected climate change scenarios.

Supplementary Information The online version contains supplementary material available at <https://doi.org/10.1007/s12237-023-01288-6>.

Acknowledgements We acknowledge the Bureau of Meteorology (Australia) for providing tidal gauge datasets, the USGS for providing Sentinel-2 satellite imagery, and the volunteers (Mohamed Macki, Ryan Midgley, Luisa Schramm, Angus Houston, and Nathan Frisby) that assisted in the fieldwork.

Author Contribution Cécile Vulliet: conceptualisation, methodology, investigation, data curation, formal analyses, writing—original draft, visualisation, funding acquisition, project administration. Jack Koci: investigation, formal analyses, validation, writing—review and editing, supervision, resources. Ben Jarihani: formal analyses, validation, writing—review and editing. Marcus Sheaves: validation, writing—review and editing. Nathan Waltham: conceptualisation, validation, visualisation, writing—review and editing, supervision, resources.

Funding Open Access funding enabled and organized by CAUL and its Member Institutions Holsworth Wildlife Research Endowment, 2021 Round 1, Cécile Vulliet, James Cook University, Competitive Research Training Grant 2021.

Data Availability Data are available on request from the corresponding author.

Declarations

Competing Interests The authors declare no competing interests.

Open Access This article is licensed under a Creative Commons Attribution 4.0 International License, which permits use, sharing, adaptation, distribution and reproduction in any medium or format, as long as you give appropriate credit to the original author(s) and the source, provide a link to the Creative Commons licence, and indicate if changes were made. The images or other third party material in this article are included in the article's Creative Commons licence, unless indicated otherwise in a credit line to the material. If material is not included in the article's Creative Commons licence and your intended use is not

permitted by statutory regulation or exceeds the permitted use, you will need to obtain permission directly from the copyright holder. To view a copy of this licence, visit <http://creativecommons.org/licenses/by/4.0/>.

References

- Abrantes, K., and M. Sheaves. 2009. Food web structure in a near-pristine mangrove area of the Australian Wet Tropics. *Estuarine, Coastal and Shelf Science* 82: 597–607.
- Alizad, K., S.C. Hagen, J.T. Morris, S.C. Medeiros, M.V. Bilskie, and J.F. Weishampel. 2016. Coastal wetland response to sea-level rise in a fluvial estuarine system. *Earth's Future* 4: 483–497.
- Allen, J. 1995. Salt-marsh growth and fluctuating sea level: Implications of a simulation model for Flandrian coastal stratigraphy and peat-based sea-level curves. *Sedimentary Geology* 100: 21–45.
- Anees, M.T., K. Abdullah, M.N.M. Nordin, N.N.N. Ab Rahman, M.I. Syakir, and M.O.A. Kadir. 2017. One-and two-dimensional hydrological modelling and their uncertainties. *Flood Risk Management* 11: 221–244.
- Annis, A., F. Nardi, A. Petroselli, C. Apollonio, E. Arcangeletti, F. Tauro, C. Belli, R. Bianconi, and S. Grimaldi. 2020. UAV-DEMs for small-scale flood hazard mapping. *Water* 12: 1717.
- Bacopoulos, P., S.C. Hagen, A.T. Cox, W.R. Dally, and S.M. Bratos. 2012. Observation and simulation of winds and hydrodynamics in St. Johns and Nassau Rivers. *Journal of Hydrology* 420: 391–402.
- Bishop, M.J., M. Mayer-Pinto, L. Airoidi, L.B. Firth, R.L. Morris, L.H. Loke, S.J. Hawkins, L.A. Naylor, R.A. Coleman, and S.Y. Chee. 2017. Effects of ocean sprawl on ecological connectivity: Impacts and solutions. *Journal of Experimental Marine Biology and Ecology* 492: 7–30.
- Blakely, J., W. McWilliam, and D. Royds. 2022. Extent and intensity of vehicle-use impacts within a saltmarsh conservation area under a management strategy. *Natural Areas Journal* 42: 56–68.
- Bouma, T., J. Van Belzen, T. Balke, J. Van Dalen, P. Klaassen, A. Hartog, D. Callaghan, Z. Hu, M. Stive, and S. Temmerman. 2016. Short-term mudflat dynamics drive long-term cyclic salt marsh dynamics. *Limnology and Oceanography* 61: 2261–2275.
- Bradley, M., I. Nagelkerken, R. Baker, and M. Sheaves. 2020. Context Dependence: A conceptual approach for understanding the habitat relationships of coastal marine fauna. *BioScience* 70: 986–1004.
- Bruinsma, C. 2001. Queensland coastal wetland resources: cape tribulation to Bowling Green Bay.
- Brunner, G.W. 2016. HEC-RAS river analysis system: hydraulic reference manual, version 5.0. *US Army Corps of Engineers—Hydrologic Engineering Center* 547.
- Cao, J., K. Liu, L. Zhuo, L. Liu, Y. Zhu, and L. Peng. 2021. Combining UAV-based hyperspectral and LiDAR data for mangrove species classification using the rotation forest algorithm. *International Journal of Applied Earth Observation and Geoinformation* 102: 102414.
- Casulli, V. 2009. A high-resolution wetting and drying algorithm for free-surface hydrodynamics. *International Journal for Numerical Methods in Fluids* 60: 391–408.
- Chassereau, J.E., J.M. Bell, and R. Torres. 2011. A comparison of GPS and lidar salt marsh DEMs. *Earth Surface Processes and Landforms* 36: 1770–1775.
- Colombano, D.D., S.Y. Litvin, S.L. Ziegler, S.B. Alford, R. Baker, M.A. Barbeau, J. Cebrián, R.M. Connolly, C.A. Currin, and L.A. Deegan. 2021. Climate change implications for tidal marshes and

- food web linkages to estuarine and coastal nekton. *Estuaries and Coasts* 1–12.
- Connolly, R.M., and N.J. Waltham. 2015. Spatial analysis of carbon isotopes reveals seagrass contribution to fishery food web. *Ecosphere* 6: 1–12.
- D'Alpaos, A., S. Lanzoni, M. Marani, and A. Rinaldo. 2007. Landscape evolution in tidal embayments: modeling the interplay of erosion, sedimentation, and vegetation dynamics. *Journal of Geophysical Research: Earth Surface* 112.
- Davis, B., R. Baker, and M. Sheaves. 2014. Seascape and metacommunity processes regulate fish assemblage structure in coastal wetlands. *Marine Ecology Progress Series* 500: 187–202.
- Deegan, L.A., J.E. Hughes, and R.A. Rountree. 2002. Salt marsh ecosystem support of marine transient species. In *Concepts and controversies in tidal marsh ecology* 333–365. Springer.
- Etherington, T.R. 2020. Discrete natural neighbour interpolation with uncertainty using cross-validation error-distance fields. *PeerJ Computer Science* 6: e282.
- Fagherazzi, S., G. Mariotti, N. Leonardi, A. Canestrelli, W. Nardin, and W.S. Kearney. 2020. Salt marsh dynamics in a period of accelerated sea level rise. *Journal of Geophysical Research: Earth Surface* 125: e2019JF005200.
- Fagherazzi, S., P.L. Wiberg, S. Temmerman, E. Struyf, Y. Zhao, and P.A. Raymond. 2013. Fluxes of water, sediments, and biogeochemical compounds in salt marshes. *Ecological Processes* 2: 3.
- Fernandez-Nunez, M., H. Burningham, and J. Ojeda Zujar. 2017. Improving accuracy of LiDAR-derived digital terrain models for saltmarsh management. *Journal of Coastal Conservation* 21: 209–222.
- Finotello, A., D. Tognin, L. Carniello, M. Ghinassi, E. Bertuzzo, and A. D'Alpaos. 2022. Hydrodynamic feedbacks of salt-marsh loss in the shallow microtidal back-barrier lagoon of Venice (Italy). *Water Resources Research* e2022WR032881.
- Fleri, J.R., S. Lera, A. Gerevini, L. Staver, and W. Nardin. 2019. Empirical observations and numerical modelling of tides, channel morphology, and vegetative effects on accretion in a restored tidal marsh. *Earth Surface Processes and Landforms* 44: 2223–2235.
- Ganju, N.K., M.J. Brush, B. Rashleigh, A.L. Aretxabaleta, P. Del Barrio, J.S. Grear, L.A. Harris, S.J. Lake, G. McCardell, and J. O'Donnell. 2016. Progress and challenges in coupled hydrodynamic-ecological estuarine modeling. *Estuaries and Coasts* 39: 311–332.
- Gedan, K.B., B.R. Silliman, and M.D. Bertness. 2009. Centuries of human-driven change in salt marsh ecosystems.
- Gilby, B.L., M.P. Weinstein, R. Baker, J. Cebrian, S.B. Alford, A. Chelsky, D. Colombano, R.M. Connolly, C.A. Currin, I.C. Feller, A. Frank, J.A. Goeke, L.A. Goodridge, G. Gaines, F.E. Hardcastle, C.J. Henderson, C.W. Martin, A.E. McDonald, B.H. Morrison, A.D. Olds, J.S. Rehage, N.J. Waltham, and S.L. Ziegler. 2021. Human actions alter tidal marsh seascapes and the provision of ecosystem services. *Estuaries and Coasts* 44: 1628–1636.
- Gonçalves, J., and R. Henriques. 2015. UAV photogrammetry for topographic monitoring of coastal areas. *ISPRS Journal of Photogrammetry and Remote Sensing* 104: 101–111.
- González, C.J., J.R. Torres, S. Haro, J. Gómez-Enri, and Ó. Álvarez. 2023. High-resolution characterization of intertidal areas and lowest astronomical tidal surface by use of Sentinel-2 multispectral imagery and hydrodynamic modeling: Case-study in Cadiz Bay (Spain). *Science of the Total Environment* 861: 160620.
- Goodwin, G.C., and S.M. Mudd. 2019. High platform elevations highlight the role of storms and spring tides in salt marsh evolution. *Frontiers in Environmental Science* 7: 62.
- Hall, J.W., S.A. Boyce, Y. Wang, R.J. Dawson, S. Tarantola, and A. Saltelli. 2009. Sensitivity analysis for hydraulic models. *Journal of Hydraulic Engineering* 135: 959–969.
- Hannaford, M., and V. Resh. 1999. Impact of all-terrain vehicles (ATVs) on pickleweed (*Salicornia virginica* L.) in a San Francisco Bay wetland. *Wetlands Ecology and Management* 7: 225–233.
- Hashemi-Beni, L., J. Jones, G. Thompson, C. Johnson, and A. Gebrehiwot. 2018. Challenges and opportunities for UAV-based digital elevation model generation for flood-risk management: A case of Princeville. *North Carolina. Sensors* 18: 3843.
- Hicks, F., and T. Peacock. 2005. Suitability of HEC-RAS for flood forecasting. *Canadian Water Resources Journal* 30: 159–174.
- Hladik, C., and M. Alber. 2012. Accuracy assessment and correction of a LIDAR-derived salt marsh digital elevation model. *Remote Sensing of Environment* 121: 224–235.
- Horstman, E.M., C.M. Dohmen-Janssen, T.J. Bouma, and S.J. Hulscher. 2015. Tidal-scale flow routing and sedimentation in mangrove forests: Combining field data and numerical modelling. *Geomorphology* 228: 244–262.
- Hu, T., X. Sun, Y. Su, H. Guan, Q. Sun, M. Kelly, and Q. Guo. 2021. Development and performance evaluation of a very low-cost UAV-lidar system for forestry applications. *Remote Sensing* 13: 77.
- Jarihani, A.A., J.N. Callow, T.R. McVicar, T.G. Van Niel, and J.R. Larsen. 2015. Satellite-derived Digital Elevation Model (DEM) selection, preparation and correction for hydrodynamic modelling in large, low-gradient and data-sparse catchments. *Journal of Hydrology* 524: 489–506.
- Jin, C., Z. Gong, L. Shi, K. Zhao, R.O. Tinoco, J.E. San Juan, L. Geng, and G. Coco. 2022. Medium-term observations of salt marsh morphodynamics. *Frontiers in Marine Science* 9: 988240.
- Jinks, K.I., M.A. Rasheed, C.J. Brown, A.D. Olds, T.A. Schlacher, M. Sheaves, P.H. York, and R.M. Connolly. 2020. Saltmarsh grass supports fishery food webs in subtropical Australian estuaries. *Coastal and Shelf Science* 106719.
- Johnson, D., and C. Pattiaratchi. 2004. Application, modelling and validation of surfzone drifters. *Coastal Engineering* 51: 455–471.
- Kalacska, M., G. Chmura, O. Lucanus, D. Bérubé, and J. Arroyo-Mora. 2017. Structure from motion will revolutionize analyses of tidal wetland landscapes. *Remote Sensing of Environment* 199: 14–24.
- Karim, F., A. Kinsey-Henderson, J. Wallace, A.H. Arthington, and R.G. Pearson. 2012. Modelling wetland connectivity during overbank flooding in a tropical floodplain in north Queensland, Australia. *Hydrological Processes* 26: 2710–2723.
- Karim, F., A. Kinsey-Henderson, J. Wallace, P. Godfrey, A.H. Arthington, and R.G. Pearson. 2014. Modelling hydrological connectivity of tropical floodplain wetlands via a combined natural and artificial stream network. *Hydrological Processes* 28: 5696–5710.
- Karim, F., J. Wallace, B.N. Abbott, M. Nicholas, and N.J. Waltham. 2021. Modelling the removal of an earth bund to maximise sea-water ingress into a coastal wetland. *Estuarine, Coastal and Shelf Science* 263: 107626.
- Kelleway, J. 2006. Ecological impacts of recreational vehicle use on saltmarshes of the Georges River, Sydney. *Wetlands Australia Journal* 22: 52–66.
- Kirwan, M.L., G.R. Guntenspergen, A. d'Alpaos, J.T. Morris, S.M. Mudd, and S. Temmerman. 2010. Limits on the adaptability of coastal marshes to rising sea level. *Geophysical research letters* 37.
- Kirwan, M.L., and A.B. Murray. 2007. A coupled geomorphic and ecological model of tidal marsh evolution. *Proceedings of the National Academy of Sciences* 104: 6118–6122.
- Koci, J., B. Jarihani, J.X. Leon, R.C. Sidle, S.N. Wilkinson, and R. Bartley. 2017. Assessment of UAV and ground-based structure from motion with multi-view stereo photogrammetry in a gullied savanna catchment. *ISPRS International Journal of Geo-Information* 6: 328.

- Koci, J., R.C. Sidle, B. Jarihani, and M.J. Cashman. 2020. Linking hydrological connectivity to gully erosion in savanna rangelands tributary to the Great Barrier Reef using structure-from-motion photogrammetry. *Land Degradation & Development* 31: 20–36.
- Kroon, F.J., and S. Phillips. 2015. Identification of human-made physical barriers to fish passage in the Wet Tropics region, Australia. *Marine and Freshwater Research* 67: 677–681.
- Kumbier, K., M.G. Hughes, K. Rogers, and C.D. Woodroffe. 2021. Inundation characteristics of mangrove and saltmarsh in microtidal estuaries. *Estuarine, Coastal and Shelf Science* 261: 107553.
- Kumbier, K., K. Rogers, M.G. Hughes, K.K. Lal, L.A. Mogensen, and C.D. Woodroffe. 2022. An Eco-Morphodynamic Modelling Approach to Estuarine Hydrodynamics & wetlands in response to sea-level rise. *Frontiers in Marine Science* 613.
- Li, B., J. Hou, D. Li, D. Yang, H. Han, X. Bi, X. Wang, R. Hinkelmann, and J. Xia. 2021. Application of LiDAR UAV for high-resolution flood modelling. *Water Resources Management* 35: 1433–1447.
- Liu, J., Y. Liu, L. Xie, S. Zhao, L. Dai, and Z. Zhang. 2021. A threshold-like effect on the interaction between hydrological connectivity and dominant plant population in tidal marsh wetlands. *Land Degradation & Development* 32: 2922–2935.
- Lovelock, C.E., M.F. Adame, D.W. Butler, J.J. Kelleway, S. Dittmann, B. Fest, K.J. King, P.I. Macreadie, K. Mitchell, and M. Newnham. 2022. Modeled approaches to estimating blue carbon accumulation with mangrove restoration to support a blue carbon accounting method for Australia. *Limnology and Oceanography*.
- Macreadie, P.I., M.D. Costa, T.B. Atwood, D.A. Friess, J.J. Kelleway, H. Kennedy, C.E. Lovelock, O. Serrano, and C.M. Duarte. 2021. Blue carbon as a natural climate solution. *Nature Reviews Earth & Environment* 2: 826–839.
- Marangoz, H.O., and T. Anilan. 2022. Two-dimensional modeling of flood wave propagation in residential areas after a dam break with application of diffusive and dynamic wave approaches. *Natural Hazards* 110: 429–449.
- Mardani, N., K. Suara, H. Fairweather, R. Brown, A. McCallum, and R.C. Sidle. 2020. Improving the accuracy of hydrodynamic model predictions using Lagrangian calibration. *Water* 12: 575.
- Marois, D.E., and H.A. Stecher. 2020. A simple, dynamic, hydrological model for mesotidal salt marshes. *Estuarine, Coastal and Shelf Science* 233: 106486.
- Martins, R., J. Leandro, A.S. Chen, and S. Djordjević. 2017. A comparison of three dual drainage models: Shallow water vs local inertial vs diffusive wave. *Journal of Hydroinformatics* 19: 331–348.
- McCormick, H., R. Salguero-Gómez, M. Mills, and K. Davis. 2021. Using a residency index to estimate the economic value of coastal habitat provisioning services for commercially important fish species. *Conservation Science and Practice* 3: e363.
- McNicol, I.M., E.T. Mitchard, C. Aquino, A. Burt, H. Carstairs, C. Dassi, A.M. Dikongo, and M.I. Disney. 2021. To what extent can UAV photogrammetry replicate UAV LiDAR to determine forest structure? A test in two contrasting tropical forests. *Journal of Geophysical Research: Biogeosciences* e2021JG006586.
- Minello, T.J., K.W. Able, M.P. Weinstein, and C.G. Hays. 2003. Salt marshes as nurseries for nekton: Testing hypotheses on density, growth and survival through meta-analysis. *Marine Ecology Progress Series* 246: 39–59.
- Minello, T.J., L.P. Rozas, and R. Baker. 2012. Geographic variability in salt marsh flooding patterns may affect nursery value for fishery species. *Estuaries and Coasts* 35: 501–514.
- Moffett, K.B., S.M. Gorelick, R.G. McLaren, and E.A. Sudicky. 2012. Salt marsh ecohydrological zonation due to heterogeneous vegetation–groundwater–surface water interactions. *Water Resources Research* 48.
- Mohamad, N., A. Ahmad, M.F.A. Khanan, and A.H.M. Din. 2021. Surface elevation changes estimation underneath mangrove canopy using SNERL filtering algorithm and DoD technique on UAV-derived DSM data. *ISPRS International Journal of Geo-Information* 11: 32.
- Molinari, D., K. De Bruijn, J. Castillo, G.T. Aronica, and L.M. Bouwer. 2017. Validation of flood risk models: current practice and innovations. *Natural Hazards and Earth System Sciences Discussions* 1–18.
- Morris, B.D., E. Foulsham, and D. Hanslow. 2013. *An improved methodology for regional assessment of tidal inundation hazards in NSW estuaries*. Sydney, Australia: Coasts & Ports.
- Morris, J.T., P. Sundareshwar, C.T. Nietch, B. Kjerfve, and D.R. Cahoon. 2002. Responses of coastal wetlands to rising sea level. *Ecology* 83: 2869–2877.
- Muñoz, D.F., D. Yin, R. Bakhtyar, H. Moftakhari, Z. Xue, K. Mandli, and C. Ferreira. 2021. Inter-model comparison of Delft3D-FM and 2D HEC-RAS for total water level prediction in coastal to inland transition zones. *JAWRA Journal of the American Water Resources Association*.
- Murray, N.J., T.A. Worthington, P. Bunting, S. Duce, V. Hagger, C.E. Lovelock, R. Lucas, M.I. Saunders, M. Sheaves, and M. Spalding. 2022. High-resolution mapping of losses and gains of Earth's tidal wetlands. *Science* 376: 744–749.
- Nardin, W., Y. Taddia, M. Quitadamo, I. Vona, C. Corbau, G. Franchi, L.W. Staver, and A. Pellegrinelli. 2021. Seasonality and characterization mapping of restored tidal marsh by NDVI imageries coupling UAVs and multispectral camera. *Remote Sensing* 13: 4207.
- Navarro, A., M. Young, B. Allan, P. Carnell, P. Macreadie, and D. Ierodiaconou. 2020. The application of unmanned aerial vehicles (UAVs) to estimate above-ground biomass of mangrove ecosystems. *Remote Sensing of Environment* 242: 111747.
- Nouwakpo, S.K., M.A. Weltz, and K. McGwire. 2016. Assessing the performance of structure-from-motion photogrammetry and terrestrial LiDAR for reconstructing soil surface microtopography of naturally vegetated plots. *Earth Surface Processes and Landforms* 41: 308–322.
- Olds, A.D., K.A. Pitt, P.S. Maxwell, and R.M. Connolly. 2012. Synergistic effects of reserves and connectivity on ecological resilience. *Journal of Applied Ecology* 49: 1195–1203.
- Pan, F., J. Zhu, M. Ye, Y.A. Pachepsky, and Y.-S. Wu. 2011. Sensitivity analysis of unsaturated flow and contaminant transport with correlated parameters. *Journal of Hydrology* 397: 238–249.
- Pasquier, U., Y. He, S. Hooton, M. Goulden, and K.M. Hiscock. 2019. An integrated 1D–2D hydraulic modelling approach to assess the sensitivity of a coastal region to compound flooding hazard under climate change. *Natural Hazards* 98: 915–937.
- Passeri, D.L., S.C. Hagen, S.C. Medeiros, M.V. Bilskie, K. Alizad, and D. Wang. 2015. The dynamic effects of sea level rise on low-gradient coastal landscapes: A review. *Earth's Future* 3: 159–181.
- Peterson, G.W., and R.E. Turner. 1994. The value of salt marsh edge vs interior as a habitat for fish and decapod crustaceans in a Louisiana tidal marsh. *Estuaries* 17: 235–262.
- Pinton, D., A. Canestrelli, B. Wilkinson, P. Ifju, and A. Ortega. 2020. A new algorithm for estimating ground elevation and vegetation characteristics in coastal salt marshes from high-resolution UAV-based LiDAR point clouds. *Earth Surface Processes and Landforms*.
- Pinton, D., A. Canestrelli, B. Wilkinson, P. Ifju, and A. Ortega. 2021. Estimating ground elevation and vegetation characteristics in coastal salt marshes using UAV-based LiDAR and digital aerial photogrammetry. *Remote Sensing* 13: 4506.
- Queensland, T.S.O. 2022. Storm tide data and tide predictions for Cape Ferguson monitoring site: the State of Queensland 1995–2022.
- Raoult, V., T.F. Gaston, and M.D. Taylor. 2018. Habitat–fishery linkages in two major south-eastern Australian estuaries show that the C4 saltmarsh plant *Sporobolus virginicus* is a significant

- contributor to fisheries productivity. *Hydrobiologia* 811: 221–238.
- Reid, S.K., P.E. Tissot, and D.D. Williams. 2014. Methodology for applying GIS to evaluate hydrodynamic model performance in predicting coastal inundation. *Journal of Coastal Research* 30: 1055–1065.
- Rivera-Monroy, V.H., R.R. Twilley, S.E. Davis III., D.L. Childers, M. Simard, R. Chambers, R. Jaffe, J.N. Boyer, D.T. Rudnick, and K. Zhang. 2011. The role of the Everglades Mangrove Ecotone Region (EMER) in regulating nutrient cycling and wetland productivity in south Florida. *Critical Reviews in Environmental Science and Technology* 41: 633–669.
- Rodríguez, J.F., P.M. Saco, S. Sandi, N. Saintilan, and G. Riccardi. 2017. Potential increase in coastal wetland vulnerability to sea-level rise suggested by considering hydrodynamic attenuation effects. *Nature Communications* 8: 1–12.
- Rozas, L.P. 1995. Hydroperiod and its influence on nekton use of the salt marsh: A pulsing ecosystem. *Estuaries* 18: 579–590.
- Saintilan, N., and K. Wilton. 2001. Changes in the distribution of mangroves and saltmarshes in Jervis Bay, Australia. *Wetlands Ecology and Management* 9: 409–420.
- Sampson, C.C., T.J. Fewtrell, A. Duncan, K. Shaad, M.S. Horritt, and P.D. Bates. 2012. Use of terrestrial laser scanning data to drive decimetric resolution urban inundation models. *Advances in Water Resources* 41: 1–17.
- Sanz-Ablanedo, E., J.H. Chandler, J.R. Rodríguez-Pérez, and C. Ordóñez. 2018. Accuracy of unmanned aerial vehicle (UAV) and SfM photogrammetry survey as a function of the number and location of ground control points used. *Remote Sensing* 10: 1606.
- Shaad, K., Y. Ninsalam, R. Padawangi, and P. Burlando. 2016. Towards high resolution and cost-effective terrain mapping for urban hydrodynamic modelling in densely settled river-corridors. *Sustainable Cities and Society* 20: 168–179.
- Sheaves, M., N. Waltham, C. Benham, M. Bradley, C. Mattone, A. Diedrich, J. Sheaves, A. Sheaves, S. Hernandez, and P. Dale. 2021. Restoration of marine ecosystems: Understanding possible futures for optimal outcomes. *Science of the Total Environment* 796: 148845.
- Shustikova, I., A. Domeneghetti, J.C. Neal, P. Bates, and A. Castellarin. 2019. Comparing 2D capabilities of HEC-RAS and LISFLOOD-FP on complex topography. *Hydrological Sciences Journal* 64: 1769–1782.
- Štroner, M., R. Urban, M. Lidmila, V. Kolář, and T. Křemen. 2021. Vegetation filtering of a steep rugged terrain: The performance of standard algorithms and a newly proposed workflow on an example of a railway ledge. *Remote Sensing* 13: 3050.
- Sun, C., S. Fagherazzi, and Y. Liu. 2018. Classification mapping of salt marsh vegetation by flexible monthly NDVI time-series using Landsat imagery. *Estuarine, Coastal and Shelf Science* 213: 61–80.
- Syme, W. 2001. TUFLOW-Two & Onedimensional unsteady flow Software for rivers, estuaries and coastal waters. In IEAust Water Panel Seminar and Workshop on 2d Flood Modelling, Sydney.
- Symonds, A.M., T. Vijverberg, S. Post, B.-J. Van Der Spek, J. Henrotte, and M. Sokolewicz. 2016. Comparison between Mike 21 FM, Delft3D and Delft3D FM flow models of western port bay, Australia. *Coastal Engineering* 2: 1–12.
- Taddia, Y., A. Pellegrinelli, C. Corbau, G. Franchi, L.W. Staver, J.C. Stevenson, and W. Nardin. 2021. High-resolution monitoring of tidal systems using UAV: A case study on Poplar Island, MD (USA). *Remote Sensing* 13: 1364.
- Taddia, Y., F. Stecchi, and A. Pellegrinelli. 2020. Coastal mapping using DJI Phantom 4 RTK in post-processing kinematic mode. *Drones* 4: 9.
- Tamminga, A., C. Hugenholtz, B. Eaton, and M. Lapointe. 2015. Hyperspatial remote sensing of channel reach morphology and hydraulic fish habitat using an unmanned aerial vehicle (UAV): A first assessment in the context of river research and management. *River Research and Applications* 31: 379–391.
- Temmerman, S., T.J. Bouma, G. Govers, Z.B. Wang, M. De Vries, and P. Herman. 2005. Impact of vegetation on flow routing and sedimentation patterns: three-dimensional modeling for a tidal marsh. *Journal of Geophysical Research: Earth Surface* 110.
- Temmerman, S., T.J. Bouma, J. Van de Koppel, D. Van der Wal, M. De Vries, and P. Herman. 2007. Vegetation causes channel erosion in a tidal landscape. *Geology* 35: 631–634.
- Teng, J., A.J. Jakeman, J. Vaze, B.F. Croke, D. Dutta, and S. Kim. 2017. Flood inundation modelling: A review of methods, recent advances and uncertainty analysis. *Environmental Modelling & Software* 90: 201–216.
- Thomas, B.E., and R.M. Connolly. 2001. Fish use of subtropical saltmarshes in Queensland, Australia: Relationships with vegetation, water depth and distance onto the marsh. *Marine Ecology Progress Series* 209: 275–288.
- Torio, D.D., and G.L. Chmura. 2013. Assessing coastal squeeze of tidal wetlands. *Journal of Coastal Research* 29: 1049–1061.
- Trave, C., and M. Sheaves. 2014. Ecotone analysis: Assessing the impact of vehicle transit on saltmarsh crab population and ecosystem. *Springerplus* 3: 1–9.
- Vanderklift, M.A., R. Marcos-Martinez, J.R. Butler, M. Coleman, A. Lawrence, H. Prislán, A.D. Steven, and S. Thomas. 2019. Constraints and opportunities for market-based finance for the restoration and protection of blue carbon ecosystems. *Marine Policy* 107: 103429.
- Wallace, J., N. Waltham, D. Burrows, and D. McJannet. 2015. The temperature regimes of dry-season waterholes in tropical northern Australia: Potential effects on fish refugia. *Freshwater Science* 34: 663–678.
- Waltham, N.J., C. Alcott, M.A. Barbeau, J. Cebrian, R.M. Connolly, L.A. Deegan, K. Dodds, L.A.G. Gaines, B.L. Gilby, and C.J. Henderson. 2021. Tidal marsh restoration optimism in a changing climate and urbanizing seascape. *Estuaries and Coasts* 1–10.
- Waltham, N.J., M. Elliott, S.Y. Lee, C. Lovelock, C.M. Duarte, C. Buelow, C. Simenstad, I. Nagelkerken, L. Claassens, and C.K. Wen. 2020. UN Decade on Ecosystem Restoration 2021–2030—what chance for success in restoring coastal ecosystems? *Frontiers in Marine Science* 7: 71.
- Wang, F., M. Eagle, K.D. Kroeger, A.C. Spivak, and J. Tang. 2021a. Plant biomass and rates of carbon dioxide uptake are enhanced by successful restoration of tidal connectivity in salt marshes. *Science of the Total Environment* 750: 141566.
- Wang, Q., T. Xie, M. Luo, J. Bai, C. Chen, Z. Ning, and B. Cui. 2021b. How hydrological connectivity regulates the plant recovery process in salt marshes. *Journal of Applied Ecology*.
- Warren, I., and H.K. Bach. 1992. MIKE 21: A modelling system for estuaries, coastal waters and seas. *Environmental Software* 7: 229–240.
- Wechsler, S. 2007. Uncertainties associated with digital elevation models for hydrologic applications: A review. *Hydrology and Earth System Sciences* 11: 1481–1500.
- Wilson, A.M., and J.T. Morris. 2012. The influence of tidal forcing on groundwater flow and nutrient exchange in a salt marsh-dominated estuary. *Biogeochemistry* 108: 27–38.
- Xin, P., G. Jin, L. Li, and D.A. Barry. 2009. Effects of crab burrows on pore water flows in salt marshes. *Advances in Water Resources* 32: 439–449.
- Xin, P., L. Li, and D.A. Barry. 2013. Tidal influence on soil conditions in an intertidal creek-marsh system. *Water Resources Research* 49: 137–150.
- Xin, P., A. Wilson, C. Shen, Z. Ge, K.B. Moffett, I.R. Santos, X. Chen, X. Xu, Y.Y. Yau, and W. Moore. 2022. Surface water and groundwater interactions in salt marshes and their impact on plant

- ecology and coastal biogeochemistry. *Reviews of Geophysics* 60: e2021RG000740.
- Yalcin, E. 2018. Generation of high-resolution digital surface models for urban flood modelling using UAV imagery. *WIT transactions on ecology and the environment, WIT Press. Lightning Source, UK, Great Britain* 357–366.
- Yeo, S., V. Lafon, D. Alard, C. Curti, A. Dehouck, and M.-L. Benot. 2020. Classification and mapping of saltmarsh vegetation combining multispectral images with field data. *Estuarine, Coastal and Shelf Science* 236: 106643.
- Yilmaz, K., Y. Darama, Y. Oruc, and A.B. Melek. 2023. Assessment of flood hazards due to overtopping and piping in Dalaman Akköprü Dam, employing both shallow water flow and diffusive wave equations. *Natural Hazards* 117: 979–1003.
- Zhao, Q., J. Bai, L. Huang, B. Gu, Q. Lu, and Z. Gao. 2016. A review of methodologies and success indicators for coastal wetland restoration. *Ecological Indicators* 60: 442–452.
- Zhu, X., Y. Hou, Q. Weng, and L. Chen. 2019. Integrating UAV optical imagery and LiDAR data for assessing the spatial relationship between mangrove and inundation across a subtropical estuarine wetland. *ISPRS Journal of Photogrammetry and Remote Sensing* 149: 146–156.
- Ziegler, S.L., R. Baker, S.C. Crosby, D.D. Colombano, M.A. Barbeau, J. Cebrian, R.M. Connolly, L.A. Deegan, B.L. Gilby, D. Mallick, C.W. Martin, J.A. Nelson, J.F. Reinhardt, C.A. Simenstad, N.J. Waltham, T.A. Worthington, and L.P. Rozas. 2021. Geographic variation in salt marsh structure and function for nekton: A guide to finding commonality across multiple scales. *Estuaries and Coasts* 44: 1497–1507.